Bioactive Materials 29 (2023) 177–195

Contents lists available at ScienceDirect

Bioactive Materials

journal homepage: www.keaipublishing.com/en/journals/bioactive-materials

Angiogenesis, hemocompatibility and bactericidal effect of bioactive natural polymer-based bilayer adhesive skin substitute for infected burned wound healing☆,☆☆

Mina Shahriari-Khalaji [a], Mamoona Sattar [b], Ran Cao [a,c,*], Meifang Zhu [a,**]

[a] State Key Laboratory for Modification of Chemical Fibers and Polymer Materials, College of Materials Science and Engineering, Donghua University, Shanghai, 201620, China

[b] Research Group of Microbiological Engineering and Medical Materials, College of Biological Science and Medical Engineering, Donghua University, Shanghai, 201620, China

[c] Shanghai Engineering Research Center of Nano-Biomaterials and Regenerative Medicine, Donghua University, Shanghai, 201620, China

ARTICLE INFO

Keywords:
Infected burn wound
Bioactive skin substitute
Double cross-linked
Anti-inflammation
Tissue adhesion

ABSTRACT

Thermal wounds are complex and lethal with irregular shapes, risk of infection, slow healing, and large surface area. The mortality rate in patients with infected burns is twice that of non-infected burns. Developing multi-functional skin substitutes to augment the healing rate of infected burns is vital. Herein, we 3D printed a hydrogel scaffold comprising carboxymethyl chitosan (CMCs) and oxidized alginate grafted catechol (O-AlgCat) on a hydrophobic electrospun layer, forming a bilayer skin substitute (BSS). The functional layer (FL) was fabricated by physiochemical crosslinking to ensure favorable biodegradability. The gallium-containing hydrophobic electrospun layer or backing layer (BL) could mimic the epidermis of skin, avoiding fluid penetration and offering antibacterial activity. 3D printed FL contains catechol, gallium, and biologically active platelet rich fibrin (PRF) to adhere to both tissue and BL, show antibacterial activity, encourage angiogenesis, cell growth, and migration. The fabricated bioactive BSS exhibited noticeable adhesive properties ($P \leq 0.05$), significant antibacterial activity ($P \leq 0.05$), faster clot formation, and the potential to promote proliferation ($P \leq 0.05$) and migration ($P \leq 0.05$) of L929 cells. Furthermore, the angiogenesis was significantly higher ($P \leq 0.05$) when evaluated *in vivo* and *in ovo*. The BSS-covered wounds healed faster due to low inflammation and high collagen density. Based on the obtained results, the fabricated bioactive BSS could be an effective treatment for infected burn wounds.

1. Introduction

Thermal burns are the fourth most common type of injury worldwide, after physical assault, falls, and traffic accidents. According to reports, around 11 million patients need burn-related medical care every year. Approximately 10% of those burn injury patients suffer from burns covering 30% or more of their entire body surface. Burns are also reported to cause 180,000 fatalities each year worldwide [1,2]. Burn victims with infections have a fatality rate that is twice as those without infections because dysregulated immune system increases the risk for infection in patients. According to reports, 42%–65% of burn victims die from infections, making infections the leading cause of death after burn injuries [3]. Beyond this, pro- and anti-inflammatory signals interact in a more intricate way, leading to dysregulation of the innate and adaptive

☆ All authors confirmed submitting manuscript entitled "Angiogenesis, hemocompatibility and bactericidal effect of Angiogenesis, hemocompatibility and bactericidal effect of bioactive natural polymer-based bilayer adhesive skin substitute for infected burned wound healing" in **Bioactive materials**. The authors are **Mina Shahriari-Khalaji, Mamoona Sattar, Ran Cao,** and **Meifang Zhu.** ☆☆ We all mutually confirm our consent to participate in this work and agreed for submission of the manuscript to **Bioactive materials** and that none has any conflicts of interest.Peer review under responsibility of KeAi Communications Co., Ltd.

* Corresponding author. Shanghai Engineering Research Center of Nano-Biomaterials and Regenerative Medicine, Donghua University, Shanghai 201620, China.

** Corresponding author. State Key Laboratory for Modification of Chemical Fibers and Polymer Materials, College of Materials Science and Engineering, Donghua University, Shanghai, 201620, China

E-mail addresses: 416015@mail.dhu.edu.cn (M. Shahriari-Khalaji), sattar.mamoona89@gmail.com (M. Sattar), rancao@dhu.edu.cn (R. Cao), zmf@dhu.edu.cn (M. Zhu).

https://doi.org/10.1016/j.bioactmat.2023.07.008
Received 14 May 2023; Received in revised form 5 July 2023; Accepted 5 July 2023

immune responses where the loss of the natural cutaneous barrier is the most obvious impact.

The infected burned injuries are challenging to treat for multiple reasons such as shape variety, lack of growth factors (GFs), progressive infection, larger surface area, and rigorous long-term therapy. Furthermore, traditional wound treatment strategies are reported to play a passive and mostly protective role in the process of wound healing, making them ineffective for burns. Advanced technology led to introduce various biologically active substances in new and already existing biomaterials. Bioactive wound dressings and skin substitutes (SS) outperform the trivial dressings to heal skin [4,5]. Wound dressings and SS have been extensively employed for burn wound treatment. SS are more desirable as they don't need to be changed frequently, saving time and money. On the other hand, changing the wound dressings could damage newly formed tissue and increase the risk of microbial infiltration and infection. Auto-grafts are the best choice for SS in burned areas, however their availability is limited due to large surface area of burn wounds. Additionally, secondary injury would increase the likelihood of pain and infection. Most importantly, auto-grafts lack antibacterial activity, rendering them ineffective to treat infected wounds [6].

Several natural and synthetic materials are used as SS for burned wound treatment. Among all kind of SS, hydrogels; three-dimensional hydrophilic networks, remain a gold regime as they keep the wound area moist, cool the wound surface, fill wound defect, absorb the wound exudate, and can be loaded with different bioactive agents such as GFs and antibacterial agents that release gradually [7]. Nevertheless, high water content can inhibit direct surface contact between hydrogels and tissue by forming a thin boundary layer, reducing surface energy that weakens their adhesion [8]. Hydrogen bonding between the water molecules and the adhesive groups in the hydrogels further reduces the interfacial interactions between the hydrogels and moist tissue surface. To overcome this issue, mussel-inspired materials have piqued our interest, which are reliable for achieving interfacial adhesion in erratic and dynamic conditions in nature. *Mytilus edulis*, a marine mussel, secretes a protein that promotes strong adhesion and energy dissipation to lessen the impact of waves. Adhesion to nearly any kind of organic or inorganic substance is facilitated by the adhesive proteins found in the mussel's sticky pads named 3,4-dihydroxy-L-phenylalanine (L-DOPA) [9]. L-DOPA is a catechol amino acid, found in the byssal threads that connect the adhesive pads to the mussel's body, which may penetrate water boundary layers and then interact with tissue to form sticky interactions [10–12]. Catechol grafted polymers have been used as tissue sealants, hemostatic agents, dermal tissue repair, fetal membrane repair, myocardial tissue repair, and hepatic tissue repair materials [13]. Han and Chen et al. [14,15] have synthesized an ultra-tough and self-healing catechol containing hydrogel with superior cell affinity and tissue adhesiveness and reported its great ability to promote skin tissue repair.

Nevertheless, hydrogels have indicated insufficient mechanical properties, lack of functionality, shape inadaptability, and undesirable degradation rate. It has been reported that taking advantage of both chemical and physical crosslinking could improve the mechanical properties and degradation rate of hydrogels [2]. The hydrogel could be further functionalized via adding different GFs and functional molecules, which can be shape customized through 3D printing.

Thus, an ideal SS with strong antibacterial activity, shape adaptability to the wound, favorable mechanical properties, wound healing promotion ability and adhesive nature, carrying a wide range of biologically active GFs with gradual release over time, would be patient-satisfying. In this work, we proposed a bioactive bilayer SS (BSS), where the backing layer (BL) is biodegradable, antibacterial, and hydrophobic electrospinning membrane to avoid fluid and bacterial intrusion, the inner layer or functional layer (FL) comprising 3D printed bioactive hydrogel could stick to both BL and tissue, and is capable of releasing antibacterial agent and GFs gradually. The BL in the SS aims to avoid the use of secondary dressing. Most often, cotton gauze is used for this purpose, but since it is passive and sticky, removing it may hurt newly formed tissue [16].

Alginate (Alg) is widely employed for biomedical material production and other skin treatments. However, its slow degradation rate and release as high molecular weight compounds could be challenging for the renal clearance [17]. Introduction of multiple functional aldehyde groups on backbone of oxidized Alg (O-Alg) can decrease its molecular weight and improve biodegradability [18]. Partially oxidized Alg can either be crosslinked with ions to form coordination bond or can be grafted chemically to other molecules via Schiff-base reaction through its aldehyde group and provide Alg derivatives with different functional groups. Schiff-base reaction is known as green and effective crosslinking method, which can be formed between aldehyde group of O-Alg and amine group containing molecules [19]. Carboxymethyl chitosan (CMCs), a biocompatible and biodegradable polymer, contains large number of amino groups that may interfere with the synthesis of macromolecules on the bacterial surface and change the permeability of the cell wall [20]. Xie et al. [21] have used CMCs, sodium alginate, and oxidized dextran to form a hydrogel wound dressing through Schiff-base reaction for fast hemostasis and treatment of infected wounds. Furthermore, Ma et al. [22] effectively employed O-Alg and CMCs to deliver keratin nanoparticles and nanosized-EGCG covered with silver and their functionalized injectable hydrogel accelerated the wound healing after release of integrated molecules.

Currently, platelet concentrates (like platelet rich plasma (PRP), platelet rich fibrin (PRF) and concentrated growth factor (CGF)) are considered as a reservoir of strong bioactive GFs. The first generation of these products, PRP and plasma rich in growth factors (PRGF), have been used in several clinical fields. However, there is a considerable debate regarding the biosafety of adding anticoagulants, thrombin, or calcium chloride to induce fibrin polymerization [23]. To overcome these drawbacks, PRF, a second-generation platelet concentrate that is self-clotted and set by one-step centrifugation, was presented, which provides more effective healing and longer GFs release [24]. Many studies have proven the beneficial effects of biologically active agent of PRF in tissues regeneration due to presence of wide range of GFs such as vascular endothelial growth factor (VEGF), fibroblast growth factor (FGF), transforming growth factor beta (TGF-β), hepatocyte growth factor (HGF), keratinocyte growth factor (KGF), platelet-derived growth factor (PDGF) and insulin-like growth factor (IGF) [25,26]. Platelet concentrates have been applied clinically in dermatology, pain management, sports medicine, plastic surgery, cardiology, urology, and dentistry [27]. However, their role in healing of infected burn wound was not investigated.

In this work, a physicochemically cross-linked multifunctional bioactive bilayer SS was developed for infected burn wound treatment (see Scheme 1). Schiff-base cross-linking was done between catechol-modified O-Alg and CMCs, as well as coordination cross-linking between O-Alg and gallium. PRF was also incorporated into hydrogel scaffold. Gallium was used in both FL and BL as a nonconventional antibacterial agent, with high and wide antibacterial activity. Gallium acts as a non-competitive inhibitor in bacterial cell by mimicking iron. Gallium-substituted enzymes cannot perform the regular functions of the iron-dependent enzymes, causing bacterial death. More importantly, in aforementioned condition, it is challenging for bacteria to develop resistance to gallium by decreasing uptake because doing so would also decrease iron uptake [28]. However, similar to other metal ions, high concentration of gallium can be toxic for human cells [29]. 3D printing was employed as a shape customizable technique forming a uniform hydrogel. More interestingly, 3D printed structure provides more surface area for GFs release and higher gallium ions can form coordination bond with Cat in 3D printed layers, which enables 3D printed hydrogels outperform conventional porous hydrogels. It was assumed that BL could prevent both fluid and bacterial invasion in injured area. Bioactive FL can simultaneously release antibacterial agent and GFs to kill the bacteria while promoting angiogenesis, fibroblast migration, and inflammation reduction. Following the dissolution of O-Alg in acidic pH

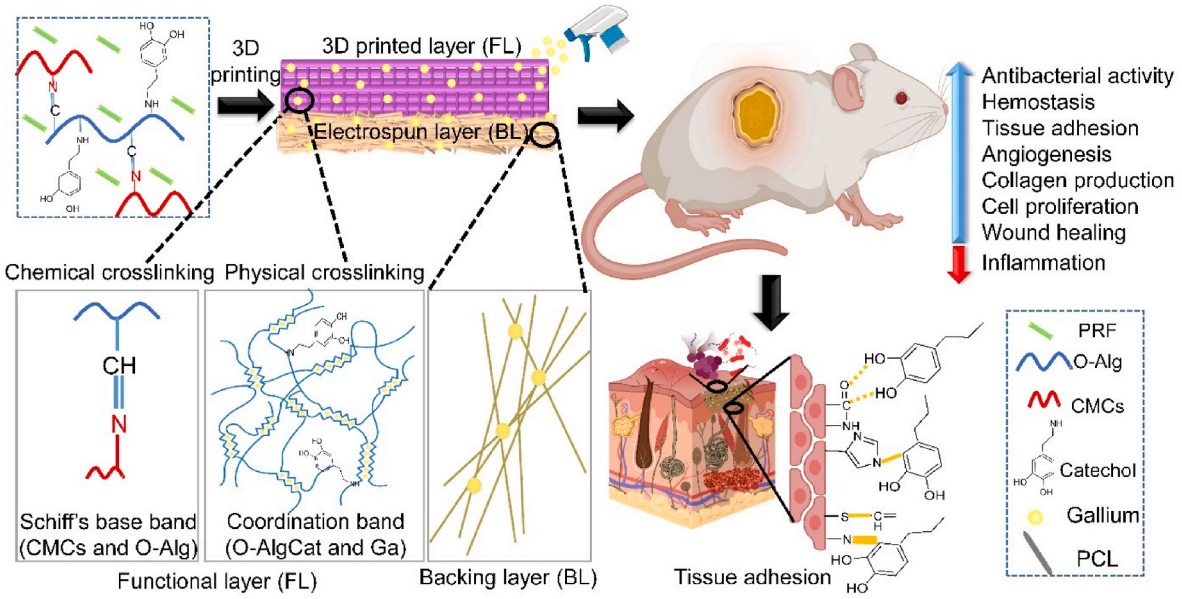

Scheme 1. Diagrammatic illustration of the multifunctional BSS's preparation approach, structure and its effect on infected burn wounds treatment.

of infected wound area, the release profile of both GFs and antibacterial agent is expected to improve. The fabricated hydrogel is envisioned to take benefit of catechol group and provide stickiness that can tightly attach to both BL and tissue.

2. Materials and methods

2.1. Materials, bacterial strains, and cells lines

All chemicals and reagents used as received without further purification. Sodium periodate ($NaIO_4$), dopamine hydrochloride (DHCl), 1-ethyl-3-(3-dimethyl aminopropyl) carbodiimide hydrochloride (EDC), *N*-hydroxysuccinimide (NHS), sodium alginate (MW = 216.121), carboxymethyl chitosan (CMCs, degree of carboxylation≥80%) were purchased form Sinopharm Chemical Reagent Co., Ltd. (Shanghai, China). Polycaprolactone (PCL, MW = 80,000) was acquired from Shanghai Macklin Biochemical Co., Ltd. Gallium nitrate was obtained from Aladdin. Urgotul silver sulfadiazine (SSD) dressing was obtained from (laboratories Urgo, France). Mouse fibroblast cells (L929 cell line) were obtained from Institute of Biochemistry and Cell Biology of the Chinese Academy of Sciences (Shanghai, China). *Escherichia coli* (*E. coli*) and *Staphylococcus aureus* (*S. aureus*) were acquired from American Type Culture Collection, Manassas, VA, USA. In whole study, double deionized water (DDW) was used.

2.2. Minimum inhibitory concentration (MIC) of gallium and backing layer (BL) fabrication

PCL was dissolved in mixture of acetic acid and formic acid (7:3) and combined with various gallium nitrate concentrations (300 μg/mL, 400 μg/mL, 500 μg/mL, 600 μg/mL, 700 μg/mL, 800 μg/mL, and 900 μg/mL). These solutions were electrospun on aluminum foil separately, with 1 mL/h feed rate under a voltage of 15 kV. PCL without gallium was also electrospun and used as control. The fabricated membranes were cut into circular shape with 1 cm diameter and sterilized via autoclave. MIC of PCL/Ga was evaluated via previously reported method [30]. Briefly, one single colony of both *E. coli* and *S. aureus* was picked up separately with a sterile loop, placed in liquid Luria-Bertani (LB) broth and put for 16 h in a shaking incubator at 37 °C. 0.2 mL bacterial suspension containing approximately 10^5 CFU/mL was directly contacted with sterile piece of material and incubated at 37 °C. The bacteria were spread on solid agar plates after 24 h with serial dilution and placed in incubator for another 16 h. The MIC was defined as the concentration at which no bacterial colonies visually appeared on an agar plate. The same procedure was used to find out the MIC of gallium in FL. Technically and biologically, each sample was triplicated. BL was fabricated via as-mentioned electrospun condition with 600 μg/mL of gallium nitrate.

2.3. PRF extraction

PRF was extracted as a method reported by Mirhaj et al. [25]. Briefly, 5 mL of blood collected form rat's retro-orbital was centrifuged at 2700 rpm for 12 min without adding any anticoagulant. Three sedimented layers were distinct after centrifugation; acellular plasma in upper layer, fibrin gel or PRF in middle layer, and red blood cells (RBCs) in bottom layer. Fibrin gel was obtained after discharging upper layer and removing bottom layer, which was freeze-dried, grinded, and stored in 4 °C for future use. In whole *in vitro* and *in ovo* studies, the above-mentioned PRF was used. Considering immune response risk for *in vivo* experiments, PRF with autologous source was extracted and used.

2.4. Alginate oxidation, catechol-grafting, ink preparation, rheological evaluations and 3D printing

Sodium alginate was oxidized following the previously reported methods [18,31]. Briefly, 2.5 g sodium periodate was dissolved in 50 mL DDW with light protection and mixed with 10 g of sodium alginate dispersed in 50 mL ethanol. After 3 h, the reaction was stopped by adding 10 mL of ethylene glycol at room temperature. Subsequently, the oxidized alginate (O-Alg) was dialyzed against DDW for 3 days before being freeze dried. Catechol grafting to oxidized alginate (O-AlgCat) was performed as reported previously by Lee et al. [32]. In brief, O-Alg (1% w/v) was dissolved in DDW followed by addition of EDC/NHS with equal molar ratio as O-Alg, the pH of mixture was set to 4.5 ± 0.5, and DHCl was added. The reaction was placed at room temperature for 12 h, dialyzed against DDW with pH 4 ± 0.2 for a day, and then freeze-dried. To confirm successful attachment of Cat to O-Alg, UV–Vis spectra of O-Alg, DHCl solution, and O-AlgCat were measured in the range of 200–500 nm using UV–Vis spectrophotometer (OPTIZEN 3220UV, Mecasys Co., Ltd.).

O-AlgCat and CMCs were run through 0.45 μm and 0.22 μm filters, separately before being mixed in 1:1 ratio, then PRF powder with

different concentrations (1, 1.5, and 2% w/v) was added and the mixture was magnetically stirred for 12 h at room temperature. For ink preparation, 1.5 w/v of PRF was used as more than this amount was insoluble in hydrogel. The rheological properties of prepared ink with and without PRF were measured via rotational rheometer (MCR 92, Anton Paar, USA) with a constant frequency of 1 Hz.

The bilayer scaffold was fabricated via printing (3D extrusion-bioprinter Bioscaffolder (Gesim, Germany) of O-AlgCatCMCsPRF on the PCL/Ga (BL) membrane at a pressure of 150 kPa and 15 mm s^{-1} front speed. Viscosity of ink was stabilized via heating the ink at 40 °C for 30 min before printing to achieve homogenous temperature distribution. The void size of the printed scaffold was set to 0.8 mm, which was the minimum void size in which stable 3D structure was achieved. The ink was then printed on BL and crosslinked with spraying gallium solution (900 μg/mL) on the FL. In the whole study, PCL/Ga was designated as BL, O-AlgCatCMCsPRF crosslinked with gallium as FL, and both FL and BL as BSS.

2.5. Oxidation degree and catechol-grafting efficiency

Degree of Alg oxidation was calculated using the iodometric titration and hydroxylamine hydrochloride method previously reported by Yuan et al. [33]. Concisely, 45% (w/v) hydroxylamine hydrochloride was dissolved in DDW containing 40 mL anhydrous ethanol, 100 mL of 4.2% sodium hydroxide (NaOH) was dissolved in ethanol, and 5 mL 0.45% bromophenol blue solution in DDW. The mixed solution was then left overnight to collect the supernatant for following quantitative analysis. O-Alg (0.1 g) was placed in a flask, then 5 mL of the above-mentioned hydroxylamine hydrochloride solution and 5 mL of anhydrous ethanol were added, and the mixture was heated to reflux for 2 h and then cooled to room temperature. The hydrochloric acid was calibrated using yellow-green 0.1 mol/L NaOH titrate solution. A similar procedure was used to carry out blank experiment without O-Alg. The degree of oxidation of the O-Alg was calculated according following equation:

$$\text{Degree of oxidation } \% = \frac{216.121 \times \mathrm{N} \times (\mathrm{V}_2 - \mathrm{V}_1)}{2\ \mathrm{W}} \times 100 \quad (1)$$

where V_1 and V_2 are the volume of hydrochloric acid added to the experimental group and blank group (L). N corresponds the concentration of hydrochloric acid used for the titration (mol/L). W refers to the weight of the O-Alg (g), while 216.12 is the molecular weight of a unit of alginate (g/mol).

The conjugation efficiency of catechol to O-Alg backbone was determined by measuring the absorbance at 280 nm using UV–vis spectrophotometer because the aromatic ring structure of conjugated catechol group exhibits absorption peak at this wavelength. DHCl solution was used to form a standard curve for catechol concentrations. O-AlgCat solution (1 mg/mL) was used as a sample [32].

2.6. BSS characterization

The freeze-dried samples were coated with a thin layer of gold before being examined with field emission scanning electron microscope (FE-SEM, Quanta FEG 250). The elemental composition of the surface was ascertained using a Shimadzu, Japan-made energy dispersive spectrometer (EDS) mapping equipment coupled to the SEM. Using Fourier transform infrared (FTIR) (FTIR-8400, Shimadzu Co. Japan) spectroscopy, the samples' molecular fingerprint was recorded with a resolution of 4 cm^{-1} in a wavenumber range of 4000–500 cm^{-1}. The hydrophilicity of the BL, PCL nanofibers, O-AlgCatCMCs-Ga, and FL was investigated via contact angle measurement. Camera and software (Wettability Pro Classic, version 2.0.0 from Czech Republic) attached to device were used to capture pictures and calculate the contact angle value. Each sample had 6 replications. D_2O was used as a deuterated reagent to evaluate the 1H nuclear magnetic resonance (1H NMR) of Alg and O-Alg at room temperature. The X-ray photoelectron spectroscopy (XPS) was studied using XPS spectrometer (Thermo Kalpha).

2.7. Tissue adhesive test and in vitro biodegradability

The adhesive strength of bioactive BSS was monitored against different substances (glass, plastic, human skin), and afterward employing porcine skin as the substrate. Adhesive and deformation strength of fabricated bioactive BSS was observed following a porcine skin bend and quantified by the slightly modified lap-shear test [7]. Fresh porcine skin was cut in rectangles (10 mm × 40 mm) and then immersed into phosphate-buffer saline (PBS) before use. O-AlgCMCs, O-AlgCatCMCs-Ga, and FL hydrogel samples (10 mm × 10 mm) were applied onto the porcine skin after excess surface PBS solution was removed. Afterward, BL (10 mm × 40 mm) was placed on the hydrogel, the bonding area was 10 mm × 10 mm. Approximately 40 min later, the tests were carried out at a rate of 5 mm/min through a universal testing machine. All of these tests were conducted thrice. Likewise, the lap-shear test was employed with FL sandwiched between either BL or pork skin to measure the adhesive strength of FL toward BL as well as pork skin. Using a universal material testing device (H5K–S, Houns field Test Equipment Ltd., England) at 25 °C and 40% humidity, the mechanical properties of BL, FL, and BSS were examined. The cross-head speed and load capacity were maintained at 50 mm/min and 100 N till rupture. Each test material was triplicated for the experiment.

In vitro degradation test was performed following a previously reported protocol by Yuan [34]. In order to simulate the physiological conditions for *in vitro* biodegradability test, O-AlgCatCMCsPRF, FL, and BSS were weighed, placed in a vial, and immersed in PBS (pH 7.4 ± 0.2) containing 1 U/mL of collagenase I and hyaluronidase. Vials were kept in water bath at 37 °C and samples were taken out of the water bath at predetermined time intervals, and weighed. The following equation was used to calculate the degradation ratio (DR%) at each time interval:

$$\mathrm{DR}\% = \frac{W_0 - W_t}{W_0} \times 100 \quad (2)$$

where W_0 and W_t were the initial weight and final weight of each sample, respectively.

2.8. Antibacterial activity and antibacterial mechanism

Direct contact method (ISO20743-2007) was used to evaluate the antibacterial activity of fabricated material against both *E. coli* and *S. aureus* as model of gram-negative and gram-positive bacteria respectively [35]. A single colony of both *E. coli* and *S. aureus* was picked up and cultivated in LB broth for 16 h at 37 °C, separately. Subsequently, 0.2 mL of each bacterial strains containing 10^6 CFU/mL was directly contacted with a piece of PCL electrospun nanofibers, BL, O-Alg-CatCMCsPRF, and FL (with diameter of 1 cm) and incubated at 37 °C for 24 h. The viable bacteria were washed out, diluted, and spread on agar plate following by incubation at 37 °C for 24 h. The number of viable bacteria were counted and reported as CFU/mL and picture of plates were captured via colony counter. Disc diffusion was carried out in accordance with the literature [36]. *E. coli* and *S. aureus* inoculum comprising 1×10^6 to 3×10^6 CFU/mL was dispersed on the agar plate separately. To determine the inhibition zone, a circular disc of sterile material was placed on the agar media and incubated for 16 h at 37 °C, followed by inhibition zone measurement. The antibacterial mechanism of both layers with and without gallium was investigated after examining bacteria via SEM. To summarize, 0.1 mL of bacterial culture was directly contacted with a piece of PCL electrospun nanofibers, BL, O-AlgCatCMCsPRF, and FL and incubated for 24 h at 37 °C. The bacteria were fixed on the surface of experimental materials after 24 h with 1 mL of 2.5% glutaraldehyde and incubated at room temperature for 4 h with light protection. Materials were rinsed with normal saline 3 times and

alcohol gradients (25%, 50%, 75%, 90%, and 100%) were used to dehydrate dressing materials, each for 15 min. Prior to freeze drying tertiary butanol was replaced with ethanol and FE-SEM was employed to observe the bacteria on the surface of samples.

2.9. Release of ion and PRF

Inductively coupled plasma-mass spectrometer (ICP-MS, Agilent 7500ce, Tokyo, Japan) was used to evaluate the release profile of gallium from FL at pH 5.5, 7.4, and 8.4 and BL at pH 7.4. PBS was prepared with different pH levels and samples with same size were immersed into PBS solution and incubated for 2, 4, 6, 8, 10, 12, 14, and 16 days with 40 rpm agitation at 37 °C. The PBS was collected at each step and replaced with fresh PBS. Platelet-derived growth factor (PDGF) and vascular endothelial growth factor (VEGF) released from synthesized material containing PRF were also measured using enzyme-linked immunosorbent assays (ELISA) kits (Zellbio, Germany), freeze dried, and fresh PRF were used as control. Briefly, 40 mg of each sample were soaked in 1 mL of Roswell Park Memorial Institute (RPMI) culture medium without serum (Gibco) followed by incubation for 2, 4, 6, 8 and 10 days at 37 °C, 5% CO_2, and 90% humidity. The culture medium was removed at each step and tested using ELISA kits and quantified by an ELISA reader (Biotek-elx 808, USA).

2.10. Blood clothing rate, hemolysis ratio, platelet and red blood cells (RBCs) observation

Whole blood clotting rate was calculated using whole rabbit blood. To sum up, 0.5 mL of $CaCl_2$ was used to recalcify the whole rabbit blood which was then directly contacted with O-AlgCatCMCs, FL, and BSS for 5, 15, 25, 35, 45, 55, and 65 min. Subsequently, 1 mL DDW was added into each sample and incubated for another 10 min at 37 °C, then the supernatant was gently removed and absorbance was measured at 550 nm using a microplate reader. Each test was biologically and technically triplicated. Platelet adhesion efficiency of samples was observed via SEM. Prior to experiment, samples were dipped in PBS for an hour at 37 °C. PRP (platelet rich plasma) was obtained by centrifuging whole rabbit blood at 100×*g* for 15 min, after which 1 mL of the obtained PRP was directly contacted with samples and incubated for 1 h at 37 °C before being fixed and observed as described in section 2.8. Hemolysis ratio was calculated as described previously [37]. In short, whole rabbit blood was centrifuged for 10 min at 116×*g* at 25 °C in order to obtain erythrocytes, then the samples were placed in 24-well plates and incubated for an hour with 1 mL PBS. Subsequently, PBS was removed, DDW was added into well as control positive, and normal saline solution was added into wells containing as-prepared samples and control negative. Obtained erythrocytes were washed thrice with PBS and directly contacted with experimental materials as well as negative and positive control. The 24-well plate was incubated in 37 °C, after 2 h the supernatant was gently transferred into tube and centrifuged at 115×*g* for 15 min. The absorbance of the obtained supernatants was measured by microplate reader at 550 nm and hemolysis ratio was calculated according to following equation:

$$\text{Hemolysis rate}\% = \frac{(\text{ODd} - \text{ODn})}{(\text{ODp} - \text{ODn})}\ \text{x100} \tag{3}$$

where ODd indicated the absorbance value of the as-prepared material, while ODp and ODn were the absorbance value obtained from positive and negative control, respectively.

Samples were soaked in PBS at 37 °C for 1 h to observe erythrocyte shape and accumulation. Then, 1 mL whole rabbit blood was added to each well, followed by incubation at 37 °C for 1 h. Cells fixation and observation were carried out as previously stated in section 2.8.

2.11. In ovo angiogenesis

To assess the angiogenic capacity of wound dressings, the chick chorioallantoic membrane (CAM) experiment was carried out. Fertilized eggs were initially incubated at 37 °C and 55% humidity for five days (Rcom MARU DELUXE MAX, South Korea). Every 12 h during incubation, the eggs were turned. After five days, the eggshell was punctured (1 cm^2), and the CAM was covered with a wound dressing (0.5 cm^2). The parafilm-covered window was then placed on each egg, which was subsequently incubated once more until day 10. For the experiment, each sample was tripled and the undressed eggs served as the controls. The eggs were removed from the incubator on day 10 of incubation, and each egg's shell was gently cracked. CAMs were fixed with 4% formaldehyde, stained with Masson's trichrome, and the slides were photographed under an optical microscope (BX51, Olympus, Japan).

2.12. In-vitro cytocompatibility and cell migration

Cytotoxicity and cell viability of the L929 mouse fibroblast cells was assessed in direct contact with O-AlgCMCs, O-AlgCatCMCs-Ga, and BSS using CCK-8 (Cell Counting Kit-8) and fluorescence Calcein AM assay reagents. DMEM (Dulbecco's Modified Eagle Medium) culture medium containing 10% FBS (fetal bovine serum) and 1% antibiotic (a mixture of penicillin/streptomycin) was used to soak the samples in a 24 well plate. Fibroblasts of concentration 1×10^4 were placed on the synthesized materials and incubated at 37 °C and 5% CO_2, whereas the culture medium was changed on daily basis. Medium was removed at day 1, 3, and 5, and PBS was used to wash the materials three times and CCK-8 (10%) was added to the surface of samples followed by incubation at 37 °C. The supernatant was collected in 96 well plate after an hour and absorbance was measured by a microplate reader at 450 nm. Fibroblasts on the surface of material at day 1, 3, and 5 were observed using fluorescence Calcein AM assay reagent. Briefly, culture medium was removed, cells on the surface of samples were washed with PBS three times and fluorescence Calcein AM assay reagent was added on the surface of samples followed by 0.5 h incubation at 25 °C. A fluorescence microscope (Olympus BX53, Japan) was employed to observe the viable cells.

Scratch tests was performed to observe mobility and migration of L929 cells in the presence of O-AlgCatCMCs-Ga, and BSS. Fibroblast cells (8×10^5) were seeded in plates and cultured using aforementioned complete growth medium containing 10% FBS, after 16–24 h monolayer cells were formed. Monolayer cells were scratched with a 10 μL pipette tip and cell debris were removed. Subsequently, the sterilized O-AlgCatCMCs-Ga and BSS (1×1 cm^2) were placed on the scratched area and the group without hydrogel was considered as control. Cells' mobility was monitored for 10 h. Cell proliferation can interrupt the mobility and migration of L929 cells, so the medium containing 0.1% FBS was used to overcome this problem. According to some reports, a medium containing 0.1% FBS can prevent cell proliferation and ensure that *in vitro* wound closure caused solely by cell migration [38]. Photos of cell scratches were taken using an inverted fluorescence microscope (IX53, Olympus) after removing hydrogels and media. Each group had three replicates. The cell mobility was calculated by the following formula:

$$\text{Cell mobility}\ (\%) = \frac{S_0 - S_t}{S_0} \times 100\% \tag{4}$$

S_0 and S_t are the initial wound area and wound area after 2, 6, and 10 h respectively.

2.13. Animal model healing and histomorphological analysis

A week before surgery, all male Sprague-Dawley rats with the average weight of 420 ± 84 g were single-housed in laboratory at 12 h light-dark cycle with free access to food (standard chow diets) and water. The animal study in this research was conducted strictly

following the Laboratory Animal Ethics Review Committee of Donghua University (DHUEC-MOST-2021-06). The operation experiment was carried out in a clean, germ-free environment. Briefly, following a 0.4 mg/kg body weight chloral hydrate injection to induce anesthesia, the dorsal side of rats was shaved and washed after cleaning with 70% alcohol. Full-thickness wound with a diameter of 0.7 mm on the dorsal area was created and stainless-steel cylindrical rod (with weight of 200 g) was used to transform it into burn wound. Stainless-steel cylindrical rod was heated in boiling water for 1 h and contacted with wound for 30 s [39]. Infection was induced via 20 μL of *E. coli* and S. *aureus* mixture in PBS with 10^7 CFU/mL final concentration [37]. Wounds were covered with SSD (commercial product for burn wound treatment), and BSS, a group without treatment was also monitored as control, healing rate of all three groups were monitored over time. The wounds were photographed throughout the experiment the healing rate was calculated as per following equation:

$$\text{Healing rate}\% = \frac{(\text{aread0} - \text{areadn})}{\text{aread0}} \times 100 \quad (5)$$

where aread0 represents the wound's size on day 0 and areadn corresponds to its size on day n. On days 6 and 12, the whole tissue around the wound was removed and submerged in a 4% paraformaldehyde (PFA) solution for Histomorphological and Immunohistochemical study. The tissue was stained using Masson's trichrome and hematoxylin-eosin (H&E) staining. Immunohistochemical staining was used to track the inflammatory response, where expressions of VEGF and cytokine were detected. Additionally, harvested tissue was stained via interleukin-6 (IL-6, Proteintech, 66,146-1-lg) and tumor necrosis factor-α (TNF-α, Abcam, ab1793). Nuclei were labeled with 4, 6-diamidino-2-phenylindole (DAPI) mounting medium, and the produced slides were observed using caseviewer software.

2.14. Static analysis

A paired Student's t-test was used for statistical analysis in this study and the data presented in the current study are mean ± standard deviation (SD). In the case of data more than two groups one-way analysis of variance (ANOVA) was employed and a p-value of ≤ 0.05 was considered significant.

3. Results and discussion

3.1. Design and structural characterization of BSS

In view of the infected burn wound requirement, a BSS containing bioactive substance was designed to deliver wide range of GFs and provide significant antibacterial activity. A hydrophobic, antibacterial, biodegradable BL was designed to enhance mechanical properties while avoiding fluid and bacterial penetration into the wounded area. Furthermore, no secondary dressing was used in the presence of this BL, which could be a promising point because removing secondary dressing (mainly cotton gauze) results in removal of newly formed tissue and a delay in healing [16]. CMCs and Alg were chosen as biocompatible, nontoxic fundamental materials for FL fabrication, as well as their ability to gradually degrade and release GFs (bioactive molecules). Prior to being grafted with Cat, Alg was partially oxidized. It has been widely reported that O-Alg with lighter molecular weight applies less pressure on renal clearance system [17]. Oxidation reaction of Alg was carried out in the presence of periodate and degree of oxidation was calculated via hydroxylamine hydrochloride method to be 8%. Bouhadir et al. [18] and Distler et al. [40] have synthesized O-Alg with sodium periodate but estimated its degree of oxidation via measuring the percentage of sodium periodate that was consumed. They reported oxidation degree to be ~5%, 13% and 19% (when 6.25 mmol and 9.375 mmol sodium periodate was used), which is in accordance with our result and slight variation can be explained by the difference in measuring methods. Both of mentioned above reports noted that the fabricated O-Alg could form coordinate bond with metal cations [18,40]. The linkage between C-2 and C-3 in the uronate unit is broken by Alg oxidation, resulting in the formation of a dialdehyde group (Fig. 1a). This ring opening in uronate unit is reported to decrease the inter/intra-molecular hydrogen bonding [41]. Sodium alginate could dissolve gradually in water and form a hydrogel that was less viscous after oxidation, which was consistent with our observation that ring opened O-Alg has better water-solubility and lower viscosity than sodium alginate solution (Fig. 1b) [42]. Cat was grafted to O-Alg with grafting efficiency of 6 ± 1%. Intriguingly, Cat grafting transformed the color of O-Alg to brown solution, visually confirming Cat conjugation to O-Alg. Lee et al. [32] have reported that DHCl concentration can increase Cat conjugation efficiency; they noted 5.5 ± 0.1% Cat conjugation efficiency to Alg with a molar ratio of 1:1, which is coherent with our results. To achieve this, carboxyl groups of Alg were activated through carbodiimide coupling chemistry (EDC/NHS chemistry), and then amine group of dopamine in DHCl was coupled to the activated carboxyl group. UV–Vis spectroscopy of O-Alg, O-AlgCat, and DHCl confirmed presence of the Cat in O-AlgCat backbone where no peak was detected in O-Alg but an obvious peak was observed at approximately 280 nm in UV spectra of both DHCl, and O-AlgCat, confirming the successful grafting of dopamine onto O-Alg (Fig. 1c) [2].

Elemental composition was characterized using XPS. The XPS survey spectrum showed the existence of carbon, nitrogen, oxygen, and gallium without impurity peaks in FL (Fig. 1d). According to C 1s XPS spectra presented in Figure S 1.a, the pronounced peak at 284.87 eV can be assigned to induced C═C bonds, while the less intensive peak at 287.76 eV corresponds to C═O bonds. A peak observed at 285.91 eV was assigned to *N*–C bonds [43]. O 1s spectra of samples exhibit a dominant peak, corresponding to the binding energy of 532.75 eV (Fig. S 1. b), which are assigned to the oxygen groups. The shoulder at the higher energy (531.8 eV) is attributed to the surface hydroxyl groups (−OH). The -C–NH– bond and the -C-NH_2 bond, respectively, are represented by binding energies of 398.91 eV and 399.63 eV in XPS curves (Fig. S 1. c) [19]. Additionally, a peak at 401.0 eV is attributed to the change in the electronic environment of the nitrogen atom caused by coordinate bond which only appeared at FL verifying coordinate bond formation (Fig. S 1. c) [7]. XPS spectra of Ga 3 d indicated a distinguishable peak at 25.54 eV only in FL as a result of presence of gallium as expected (Fig. S 1. d).

The chemical structures of initial and fabricated materials in different stages were characterized by FTIR spectroscopy. Peaks at 2927 cm^{-1}, 1025 cm^{-1}, and 1597 cm^{-1} in Alg spectra were attributed to stretching vibration of C–H, *C*–O–C, and COO^-, respectively (Fig. 1e) [44]. A peak observed in absorption spectrum of O-Alg at 1730 cm^{-1} was absent in Alg, which is a finger print of aldehyde group, confirming successful oxidation of Alg [21]. Moreover, in O-Alg, a peak at 813 cm^{-1} was weakened compared with Alg, which could be because of breakage of C–C of adjacent hydroxyl groups. Blue-shift in absorption of –OH at 1297 cm^{-1} to 1317 cm^{-1} and its weakening indicates the oxidation of adjacent hydroxyl groups in O-Alg (Fig. 1e) [45]. Following catechol grafting to O-Alg, a series of new peaks appeared at 1618 cm^{-1}, 1594 cm^{-1}, 1512 cm^{-1}, and 1468 cm^{-1} ascribing to stretching vibrations of the aromatic ring ν(C–C)/ν(C═C) and stretching vibrations of the phenolic group ν(C–OH) at 1279 cm^{-1}, 1254 cm^{-1} and 1239 cm^{-1}, bending vibrations of the phenolic group δ(C–OH) at 1365 cm^{-1}, 1184 cm^{-1}, 1163 cm^{-1}, and 1149 cm^{-1} and bending δ(C–H) at 1039 cm^{-1} and 1093 cm^{-1} (Fig. 1e) [46].

After CMCs' addition, two absorptions between 3400 cm^{-1} and 3500 cm^{-1} appeared, corresponding to the symmetric and asymmetric stretching vibration of N–H in CMCs. Furthermore, imine bond's peak appeared at 1645 cm^{-1} confirmed Schiff-base bond (Fig. 1e) [47]. The amino groups in CMCs and the aldehyde groups in O-Alg formed Schiff-base bonds (Fig. 1a), which was confirmed visually by hydrogel formation (Fig. 1b) and chemically via FTIR spectral peak of 1645 cm^{-1} (Fig. 1e).

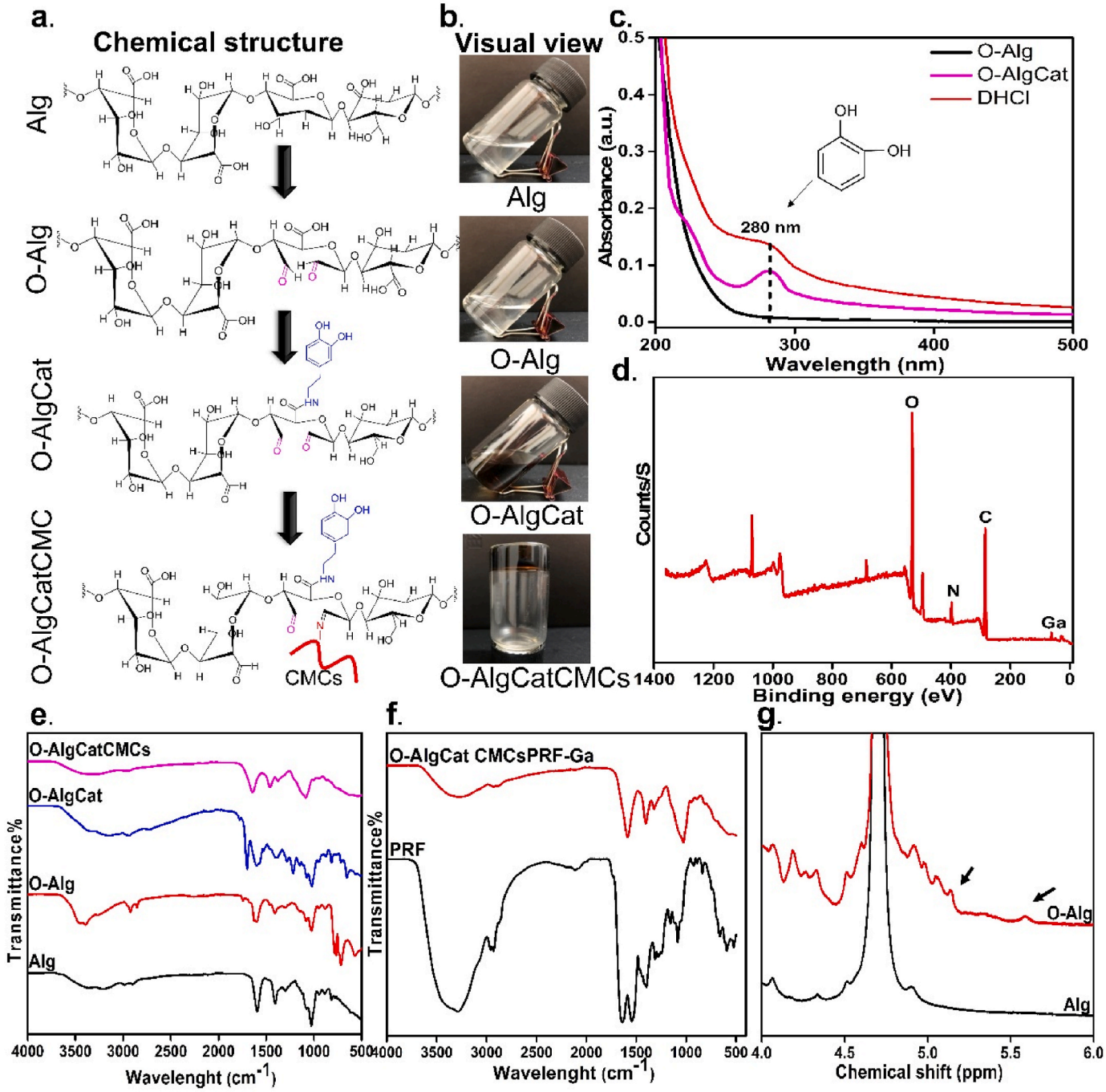

Fig. 1. Preparation and characterizations of O-AlgCatCMCs hydrogel. (a) Chemical structure and (b) Visual view of Alg, O-Alg, O-AlgCat and O-AlgCatCMCs, (c) UV absorption spectra of O-Alg, O-AlgCat and DHCl, (d) XPS survey of FL, (e) FTIR spectra of Alg, O-Alg, O-AlgCat and O-AlgCatCMCs, (f) FTIR spectra of PRF and O-AlgCatCMCsPRF, and (g) HNMR spectra of Alg, and O-Alg.

The PRF exhibited three main peaks as a PRF finger print at 1676 cm^{-1}, 1556 cm^{-1}, and 1431 cm^{-1}, corresponding to amide I: C═O tensile vibrations, amide II: N–H flexural vibrations in the plane and C–N tensile vibrations, and amide III: C–N tensile vibrations [26]. FTIR spectra of FL confirmed Schiff-base bond between O-Alg and CMCs due to peaks at 1630 cm^{-1}, indicating the successful formation of Schiff-base and also the absence of aldehyde. Additionally, the peak referring primary amide of PRF also disappeared, indicating that PRF may also have Schiff-base reaction with O-Alg (Fig. 1f). Moreover, HNMR data indicated two additional signals appeared roughly at 5.6 and 5.08 ppm in the spectra of O-Alg due to a hemiacetalic proton generated from an aldehyde and nearby hydroxyl groups, confirming successful oxidation of alginate (Fig. 1g).

3.2. Hydrogel characterization, BSS fabrication, and adhesive property

To fabricate bioactive BSS, O-AlgCatCMCsPRF hydrogel was printed on electrospun layer of PCL-Ga (BL), and the gallium nitrate solution was then sprayed on the FL to form coordinate bond (between O-AlgCat and Ga). The visual appearance of 3D printed FL indicated a fine uniform 3D multilayer structure with brown color as an indicative of Cat presence in hydrogel, which remained unchanged when printed on BL (white layer) (Fig. 2a).

The adhesiveness of the FL of BSS toward different substance was

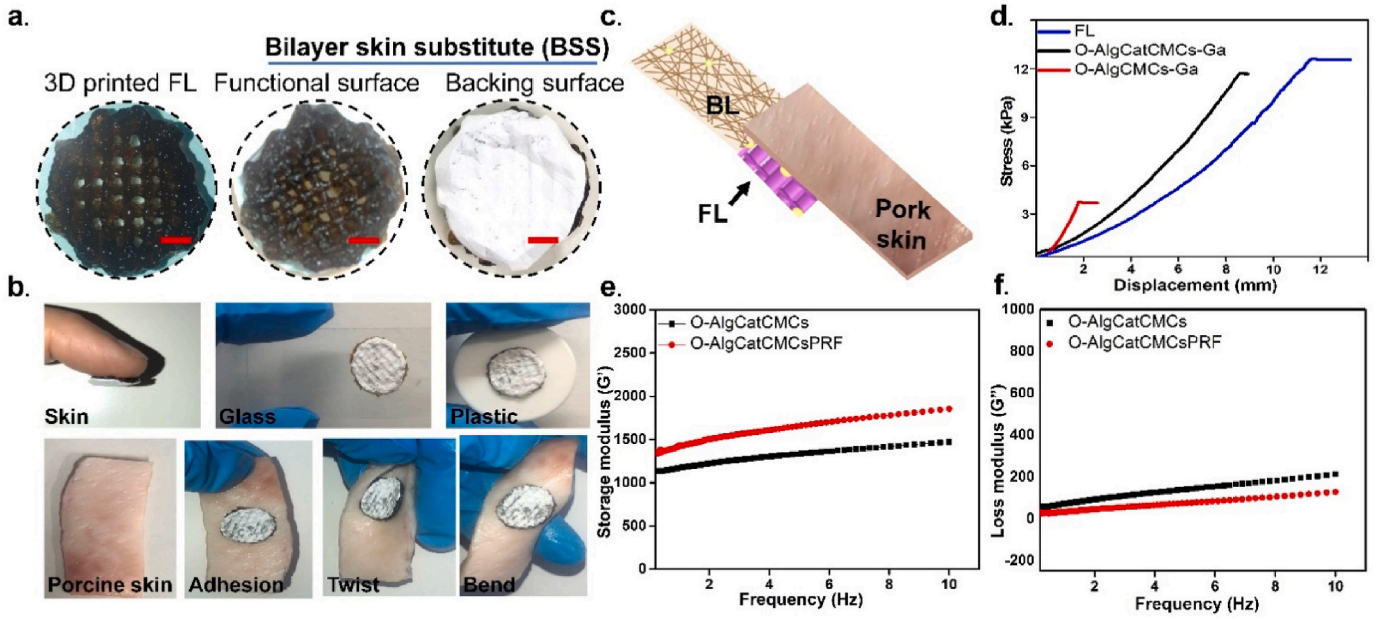

Fig. 2. The visual appearance and shear strength of BSS. (a) Visual images of the 3D printed FL, and functional and baking surface of BSS (Scale bar = 2 mm), (b) Adhesion of FL of BSS on different substitute and pig skin under twisted and bent conditions, (c) Schematic diagram of slightly modified lap-shear test on pig skin, (d) The strain-stress curve of the overlapping lap-shear test, (e) Rheological characterizations of the hydrogels, showing the (e) storage modulus (G′), and (f) loss modulus (G″) against frequency.

observed and the results confirmed high tendency of fabricated BSS toward firm adhesion to different substances such as glass, plastic, pork skin, and human skin without any external assistance (Fig. 2b). It was also detected that the adhesion is strong enough to withstand bent and twisted porcine skin, without any deformation or detachment observed (Fig. 2b). The adhesion of FL was further tested via forward moving human skin, which demonstrated tight adhesion to both human skin and BL (Movie S 1). This finding could be promising for dynamic wounds with high frequency movement such as elbow and knee joints because FL provides a stable connection between tissue and the BL. Lap-shear measurements with minor modifications were made to evaluate adhesive behavior of synthesized O-AlgCMCs-Ga, O-AlgCatCMCs-Ga, and FL (Fig. 2c) [7]. When O-AlgCMCs-Ga was placed in between pork skin and BL, adhesive strength of 3.3 kPa was observed. Cat-containing hydrogel showed significant increase, with 11.7 kPa and 12.2 kPa in O-AlgCatCMCs-Ga and FL, respectively (Fig. 2d). Additionally, the adhesive behavior of FL was measured when it was sandwiched between either BL or pork skin (Fig. S 2. a), the results demonstrated the adhesive strength of 14 kPa and 11 kPa, when FL was placed in between of BL and pork skin, respectively (Fig. S 2. b). The significantly higher adhesive strength ($p \leq 0.05$) of FL when it was sandwiched between hydrophobic BL, could be explained as high affinity of catechol group for hydrogen bonding with hydrophobic surfaces [48]. In addition of hydrogen bonding, catechol interacts with different surfaces through π– π stacking, coordination bond, and covalent bonding with surface amines [48]. Low shear strengths in O-AlgCMCs-Ga could be explained by hydrogen bonding between polar groups (such as –CONH and –OH) in pork skin and hydrogels (-OH and –CHO) [21]. However, it has been reported that the presence of fluid in physiological conditions reduces the interfacial interactions between the hydrogels and moist tissue surfaces due to the formation of hydrogen bonds between the water molecules and the adhesive groups in hydrogels [8]. Higher shear strengths in O-AlgCatCMCs-Ga, FL could be clearly attributed to the presence of Cat group, which has been reported to potentially increase adhesive force and further strengthen adherence [49].

The fracture stress, Young's modulus, and breaking elongation of FL, BL and BSS are summarized in Table S1. The data show that BSS had the highest fracture stress, elongation at break and Young's modulus of 4.84 MPa, 84% and 1.06 MPa, respectively. Fracture stress, elongation at break and Young's modulus of the BL were slightly lower than BSS, which was noticeably higher than FL.

Fig. 2e and f presents the storage modulus (G') and loss modulus (G") against frequency. The stability of O-AlgCatCMCs hydrogel with and without PRF was examined in relation to the cured systems' gel properties using the rheological frequency sweep from 0.1 to 10 Hz. The obtained mechanical spectra demonstrated that, for both of the hydrogels, the storage moduli G′ are significantly greater than the loss moduli G″ and that G′ exhibited a stationary state in the range of 0.11 Hz, which are characteristics for a well-developed network [50]. Addition of PRF enhanced storage modulus and slightly reduced loss modulus.

3.3. Physical properties of the hydrogels

The microstructure of all the 3D printed hydrogels had an irregular porous structure, which can ensure the capability to transport nutrient substance and oxygen through tissue. O-AlgCMCs with single Schiff-based band exhibited highly porous and microfiber structure with 80 ± 3 μm pore diameter. O-AlgCMCs-Ga benefits from both Schiff-base bond and coordination bond; however, gallium addition influenced the microstructure by reducing porosity and increasing pore size to 92 ± 4 μm, which can be ascribed to the formation of egg-box model [51]. Alginate is partially oxidized with 8% degree of oxidation, implying that the remaining carboxyl group could be physically crosslinked with gallium. The addition of Cat to O-AlgCatCMCs further reduced the pore size to 67 ± 2 μm that could be due to sticky nature of Cat. Due to presence of PRF, which has been reported to have a fibrin matrix and double cross-linked structure of the Schiff-base and coordination bond, the pore size of the FL hydrogel was the smallest (63 ± 10.16 μm) [52]. It is evident that both Schiff-base and coordination bond directly affected the pore diameter and frequency (Fig. 3a and b). PCL electrospun nanofibers with and without gallium indicated a typical electrospun nanofiber structure with ultra-fine drop-less fibers. The PCL electrospun nanofibers indicated smooth fibers with 2.33 ± 0.43 μm diameter, whereas fiber diameter slightly increased (2.47 ± 0.5 μm) in hybrid PCL-Ga (FL) fibers that exhibited rough surface caused by gallium addition (Fig. 3c). Element analysis result revealed that carbon and

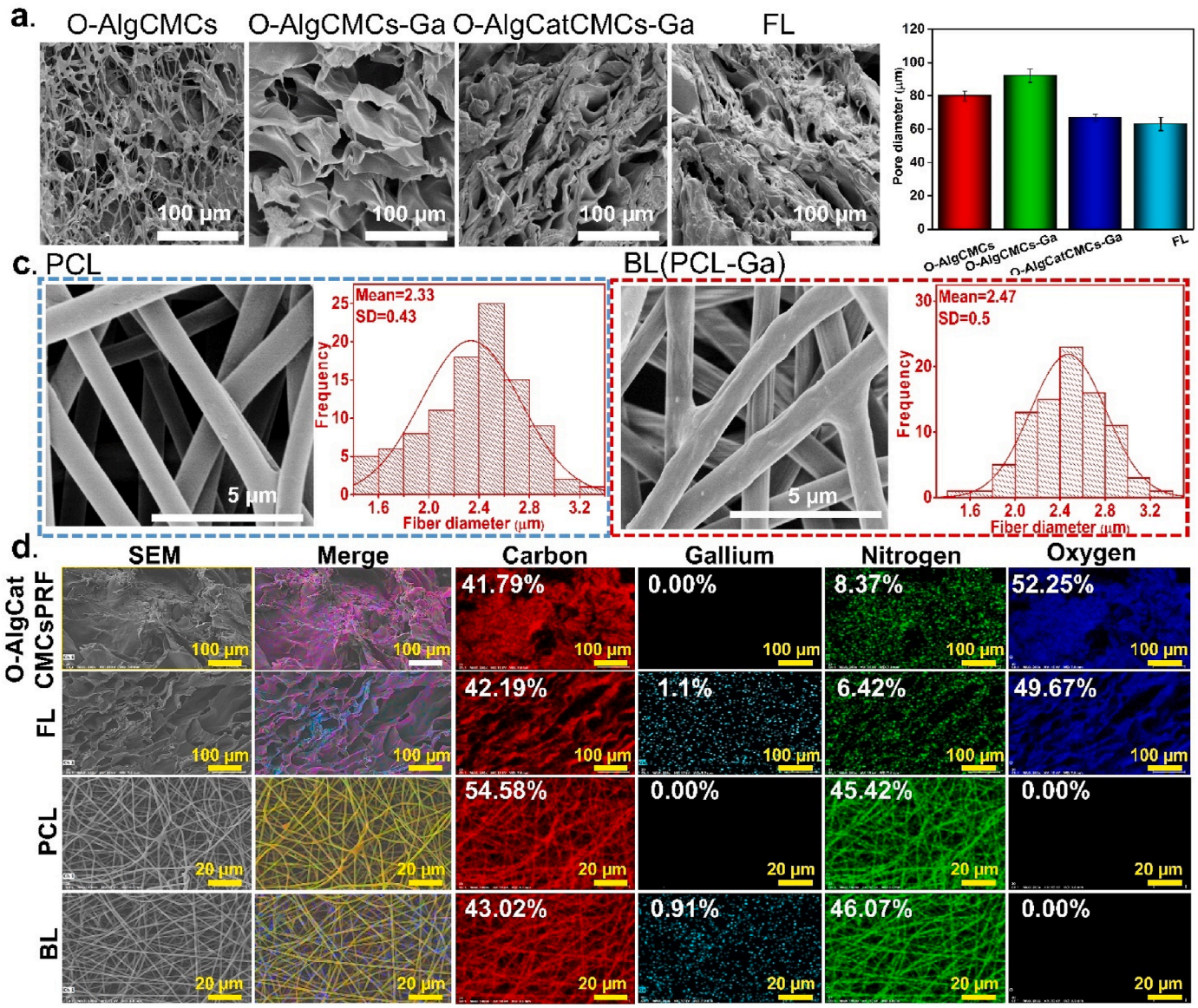

Fig. 3. Microstructure of fabricated BSS and its BL and FL. (a) SEM image of different state of FL, (b) Pore size diameter of different state of FL, (c) PCL nanofibers and BL nanofibers and their fiber diameter, (d) Element distribution of different state of FL and BL.

nitrogen were well distributed in both PCL and O-AlgCatCMCsPRF. In addition to the elements mentioned above, the uniform distribution of gallium was also confirmed in FL and BL. A sparing technique was used to distribute gallium ion on O-AlgCatCMCsPRF and uniform gallium distribution suggests effectiveness of spraying method which can be used for similar purposes (Fig. 3d).

3.4. Antibacterial capability and mechanism

The MIC of gallium in BL was found to be 500 μm/mL against *E. coli*, while 600 μm/mL against *S. aureus*. The MIC was slightly higher in FL, which was 800 μm/mL and 900 μm/mL against *E. coli* and *S. aureus*, respectively. According to Xu et al. [53] the MIC of gallium nitrate solution toward *E. coli* and *S. aureus* was 256 and 512 μm/mL, respectively, confirming the high antibacterial activity of gallium at low concentration. The difference in MIC reported by Xu et al. [53] and our study could be explained in terms of different bacterial strains, experimental conditions, and most importantly use of gallium nitrate solution by Xu et al. It is worth noting that the MIC value was higher in FL in comparison to BL after 24 h of direct contact with bacterial strains. This fact could verify the presence of gallium in coordination bonds of O-Alg, which can be released by degradation of FL over longer time period than 24 h, as confirmed by release profile and biodegradability rate (Fig. 4e and Fig. S6a).

The exudate secretion of burned wound is reported to be higher than other wounds, providing an ideal environment for germs' multiplication. This scenario gets exacerbated in infected burned wounds, where the amount of exudate is much higher and can easily transform into chronic nonhealing wound. More importantly, infection has been reported to be the most common and potentially preventable obstacle to healing [54]. Therefore, antibacterial activity is crucial for the treatment of infected burned wounds. The fabrication of BSS focused both on killing of already presented bacteria in the wound and preventing bacterial penetration into wound. Thus, both FL and BL of BSS were tested against *E. coli* and *S. aureus*, and antibacterial mechanism was also investigated. The results indicated that after 24 h of direct contact with bacteria, PCL electrospun nanofibers had noticeable bacterial growth, which was significantly ($p \leq 0.001$) reduced when gallium was added to BL (around 7 log value). The FL also showed 100% killing ratio against both bacterial strains due to inclusion of gallium (Fig. 4a and b). The

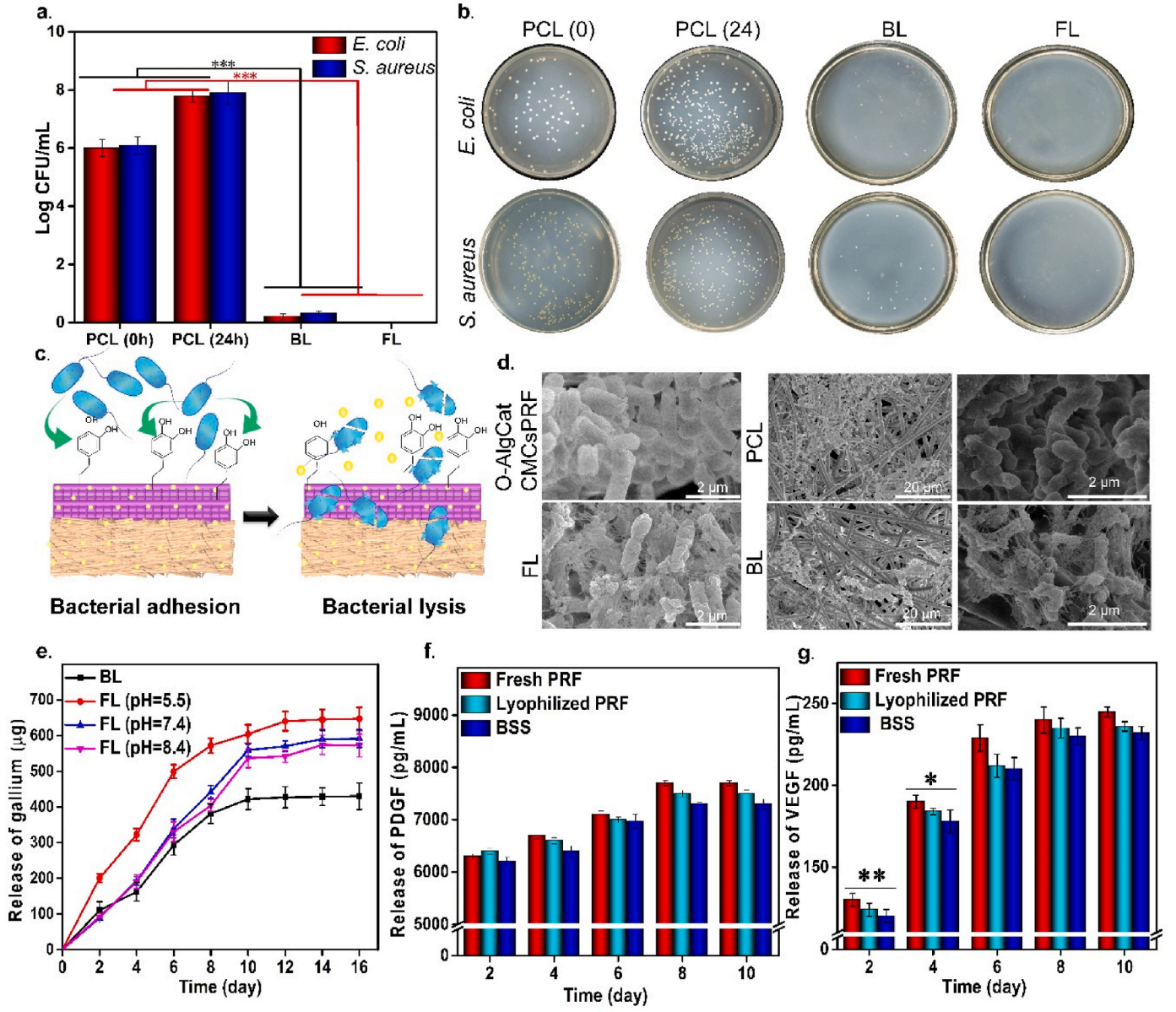

Fig. 4. Antibacterial activity and release profile of gallium from both FL and BL and GFs (VEGF and PDGF) from FL. (a) Antibacterial activity against *E. coli* and *S. aureus*, (b) Visual image of agar plates, (c) Schematic mechanism of bacterial capture via Cat and bacterial lysis by gallium, (d) SEM image of *E. coli* after 24 h direct contact with FL, BL, PCL nanofibers, and O-AlgCatCMCsPRF. (e) Release profile of gallium ion from FL in different pH of 5.5, 7.4 and 8.4 and BL, (f) Release profile of PDGF and (g) Release profile of VEGF from FL.* refers to $p \leq 0.05$, ** refers to $p \leq 0.01$, and *** refers to $p \leq 0.001$.

visual image of bacterial colonies on agar plate was also presented in Fig. 4 b. Additionally, disk diffusion method confirmed the results of direct contact method, demonstrating impressive ($p \leq 0.001$) antibacterial activity of both BL and FL (Figure S3). The 100% killing ratio of FL could be attributed to the presence of higher concentration of gallium in FL, which may not be released within 24 h in BSS and could interact with bacteria on wound surface (Fig. 4e). Intriguingly, slight antibacterial activity has been also reported for O-Alg, CMCs, and PRF, providing a synergistic effect with gallium and enhance antibacterial activity of FL [21,55]. According to reports, the Cat group in FL has a high affinity for bacterial cell capture, which could make it easier to catch germs and render them more accessible to gallium. Furthermore, gallium as a nontoxic antibacterial agent could easily penetrate into bacterial cells and destroy them (Fig. 4c) [56].

SEM images of bacteria displayed on the surface of FL (contain Ga) indicated that not only bacterial population was suppressed but also the bacterial cell membrane was damaged. The same result was obtained when bacteria were directly contacted with BL, where presence of gallium led to fragile cell wall and less bacterial growth and multiplication (Fig. 4d and Fig. S4). It has been reported that antibacterial activity of gallium is based on gallium uptake by bacteria as it mimics iron. Gallium substituted enzymes cannot perform the functions of the corresponding iron-dependent enzymes, which are essential for bacterial proliferation, because gallium is a redox inert metal that cannot be reduced under physiological conditions. As a result, iron metabolism is disrupted, resulting in bacterial death. Iron is a crucial component for bacterial growth, particularly for pathogenic germs causing illnesses. More importantly, in aforementioned condition, it is challenging for bacteria to develop resistance to gallium by decreasing uptake because doing so would also decrease iron uptake [28]. It is worth nothing that taken benefit of cell affinity of Cat group, the fabricated bioactive BSS exhibited a great advantage over the most traditional hydrogels with cell-repellent behavior.

The contact angle test was performed to examine wettability of the

FL and BL. Contact angle value of the PCL electrospun nanofibers and BL was 85° ± 4° and 97° ± 5°, respectively, confirming hydrophobicity of the BL, avoiding liquid penetration into wounded area (Figure S5). The higher contact angle value of the BL in comparison to PCL nanofibers can be attributable to the addition of gallium ion and slight increment in fiber diameter and lower pore size (Fig. 3c). O-AlgCatCMCs-Ga and FL were hydrophilic in nature with contact angle of 30° ± 3° and 29° ± 4°, respectively, which reflects their water absorption capacity allowing FL to effectively take in tissue exudates and keep the environment wet to promote wound healing. Addition of PRF slightly reduced the contact angle value that could be credited to high water solubility of PRF.

Degradation during the wound healing process is an essential parameter in innovative hydrogels as SS. Degradation rates of O-Alg-CatCMCsPRF, FL, and BSS were determined *in vitro*. As shown in Figure S6 a, O-AlgCatCMCsPRF has a single Schiff-base bond and it degrades completely after 7 days. However, FL with both Schiff-base and coordination bonds indicate lower degradation rate up to 10 days. The BSS was totally disintegrated after 12 days. The effect of degradation on adhesiveness was also studied. The result indicated that following degradation of FL, the adhesiveness decreased, which was not measurable after day 6 due to tiny size of the sample. This decrement could be attributed to the size reduction of FL that indicates presence of fewer Cat group resulting in lower adhesion (Figure S6b).

3.5. Accumulative release of gallium, PDGF, and VEGF

BL of BSS gradually released gallium over 10 days, while gallium release from FL had a pH-responsive pattern. The gallium was released faster in pH 5.5 than 7.4 and 8.4 (Fig. 4e). It has been widely reported that bacterial infection causes the pH of a wound environment to drop to 5.5 due to lactic acid and acetic acid synthesis during anaerobic fermentation [57–59]. More the release of gallium in infected area, higher is the antibacterial activity of synthesized BSS. FL demonstrated the potential to function as a smart biomaterial in an infected wound by increasing gallium release and enhancing antibacterial activity, which can be ideal for infected wounds treatment. We have previously cross-linked Alg with six metal cations (manganese, cobalt, copper, zinc, silver, and cerium) and assess their release in different pH, our results indicated that higher release was achieved in acidic pH (pH = 5.5) rather than neutral (pH = 7.4) and basic pH (pH = 8.4) [51]. We also conclude that Alg hydrogel behavior as well as tendency of ions to release at lower pH have active role in obtaining desired results [51]. Herein, we infer that partially oxidized Alg has the same pH-responsive ion release behavior as Alg.

Fig. 4f and g depicts the release of PDGF and VEGF as bioactive molecules from FL of BSS, fresh PRF, and lyophilized PRF powder. According to the findings, the GFs release in FL was slightly ($p > 0.05$) lower than that in fresh-PRF and lyophilized-PRF powder. Sustained release of PDGF and VEGF was observed over time. GFs can actively interact with tissue and known to be essential polypeptides with high biological activity that have direct and noticeable effect on cell growth, proliferation, migration, and metabolism. All phases of the healing process are managed by cytokines and GFs. According to the previous reports, the level of GFs in chronic wounds significantly drops. Additionally, several proteases are activated in the wound bed, diabetic wounds, chronic wound, infected wounds, and these proteases can quickly break down both naturally secreted GFs and those supplied topically or injected [60,61]. To avoid chronic wound formation and secure normal healing, secretion of biologically active GFs is of prime importance. PDGF and VEGF are considered as two most crucial GFs in the wound healing process. In the wound area, PDGF stimulates the migration of neutrophils, monocytes, and fibroblasts by chemotaxis, resultantly lowering the inflammation and promoting extra cellular matrix (ECM) especially collagen synthesis. Neutrophils and monocytes exit from vessels' walls followed by chemotaxis gradient and fight with infection during inflammatory stage of healing. The FL of BSS caused augmented release of PDGF up to 8 days, which could shorten the inflammatory step via accelerating the bacterial phagocytosis by neutrophils and macrophages. Inflammatory stage takes about 5 days [62] and continuous release of PDGF could stimulate fibroblast cells to synthesize collagen and ECM in proliferation stage of healing.

VEGF, also known as the key factor of proliferation stage and critically important for angiogenesis, encourages the migration and proliferation of endothelial cells, and development of granular tissue [60,63]. Proliferation starts from day 3 and could last for 2–3 weeks [62]. The FL of BSS releases VEGF (released from RPF) up to 10 days, which could encompass proliferation phase of healing. It has also been stated that both PDGF and VEGF promote normal wound healing and avoid chronic wound formation [63].

3.6. Hemostatic performance

The ability of BSS to aid in clot formation was evaluated in different time points, by directly contacting it with blood, where a lower clotting rate was represented by hemoglobin (Hb) with a higher absorption value. The bioactive BSS proved superior in clot formation at each time point over O-AlgCatCMCs-Ga followed by O-AlgCatCMCs (Fig. 5a). The difference of clot formation rate was obvious even in the first 5 min of direct contact of blood with bioactive BSS, which was persistent in same order after 15, 25, 35, 45, 55, and 65 min.

Platelet activation, adhesion, and aggregation are the three main processes through which platelets can induce primary hemostasis and activate prothrombin to produce fibrin more quickly and effectively. Platelet adherence is an initial step of blood clotting that is crucial for blood coagulation. Analysis of platelet adhesion and aggregation indicated that huge number of platelets adhered on the surface of FL contrary to O-AlgCatCMCs-Ga followed by O-AlgCatCMCs (Fig. 5b), which could be the possible reason of rapid clot formation by FL (Fig. 5a).

Hemolysis results revealed that hemolysis ratio of FL (0.7%) is higher than O-AlgCatCMCs-Ga (0.56%) followed by O-AlgCatCMCs (0.43%) (Fig. 5c). The acceptable homolysis ratio is reported to be lower than 5%, however, BSS indicated remarkably lower hemolysis around 0.7%. Xie et al. [21] stated that hemolysis value of AlgCMCs crosslinked oxidized dextran was lower than 2%, which was in line with our study and slight difference in values could be attributable to presence of gallium and PRF in fabricated BSS. The morphological observation of RBCs via SEM revealed that few erythrocytes burst or had morphological changes, confirming the biocompatibility of synthesized BSS toward erythrocytes (Fig. 5d). It was also clearly observed that huge number of RBCs accumulated on the surface of BSS compared to O-AlgCatCMCs-Ga followed by O-AlgCatCMCs (Fig. 5d). It could be ascribed to the presence of great number of positively charged nitrogen in PRF and CMCs that are able to interact electrostatically with negatively charged erythrocytes. The addition of gallium probably had the same electrostatic effect with RBCs (Fig. 5e). Furthermore, PRFs have fiber structure, which can trap RBCs and facilitate clot formation [64]. The hemolysis value, faster blood clot formation, impressive platelet adhesion, and gathering higher number of RBCs in the presence of the bioactive BSS confirms that the synthesized bioactive BSS could be used as a desirable and functional blood contacting material, which improves hemostasis, promoting healing.

Taken all the results of platelet activation, red blood cells accumulation, and blood clotting together, and due to the widely reported fact that adhesive hydrogels could reduce bleeding because of their stickiness, and facilitate faster clotting in bleeding wounds [2,7], we predict that BSS could outperform in wounds with hemorrhage condition. Faster clotting of BSS can be attributed to its adhesiveness, enabling it to adhere onto the hemorrhage sites and form a barrier to stop the bleeding, which can be promising as hemostatic material.

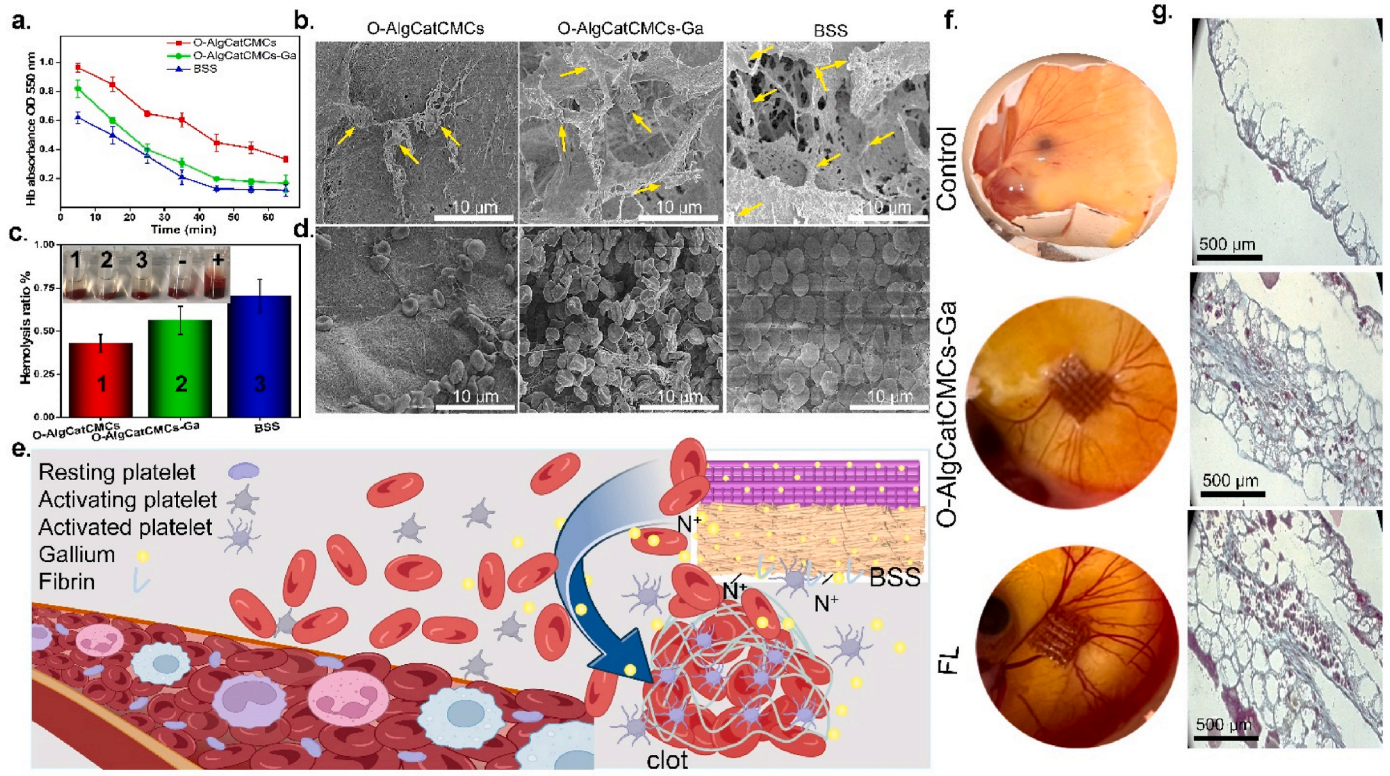

Fig. 5. (A) Blood clotting rate, (b) SEM images of platelets, yellow arrows indicate activated platelets (c) Hemolytic ratio, (d) SEM images of RBCs, (e) Clot formation mechanism in the presence of BSS, (f) Visual image of the angiogenic potential determined by CAM test and (g) Masson's trichrome-stained histological pictures of CAMs associated with control, O-AlgCatCMCs-Ga and FL.

3.7. In ovo angiogenesis evaluation

Angiogenesis is a process of creating new blood vessels from existing capillaries, which is crucial to inflammatory processes and repair of injured tissues. Angiogenesis is known as a tightly controlled biological process wherein endothelial cells proliferate, migrate, and form a tubular structure. Regeneration of blood vessels to establish vascular networks and deliver nutrients and oxygen to the cells at the wound site is one of the most crucial elements in the wound healing process [26]. CAM assay is widely used technique to evaluate angiogenesis potential of biomaterials. It has been reported that the chick immune system is not developed in first two week, which could be functional after almost 18 days [25,65]. To assess the angiogenic potential of O-AlgCatCMCs-Ga, and FL, the CAM test was carried in almost 2 weeks. The eggs treated with FL had more blood vessels developed in comparison to control and O-AlgCatCMCs-Ga (Fig. 5g). The presence of PRF expedited blood vessel creation and boosted angiogenesis potential as evidenced by the presence of more blood vessels surrounding FL than control and O-AlgCatCMCs-Ga. The enhanced angiogenesis potential of FL could be attributed to the release of growth factors, and the ECM-like scaffold structure.

VEGF is a strong bioactive angiogenic growth factor and one of the most significant growth factors present in PRF to bring on the endothelial mitogenic response. Additionally, it has been demonstrated that the fibrin matrix interacts with fibroblasts and epithelial cells and enhances angiogenesis [66]. On the other hand, prior studies have shown that high hydrophilic biomaterials can induce blood coagulation, ECM protein absorption, as well as the expression of several genes involved in angiogenesis. According to Ziebart et al. [67], highly hydrophilic surfaces can promote the development of undifferentiated endothelial progenitor cells, which in turn can lead to production of pro-angiogenic substances including VEGF-A, eNOS, and iNOS. Hence, the increased hydrophilicity of these scaffolds may be another factor influencing the rise of angiogenesis potential in FL and O-AlgCatCMCs-Ga.

Masson's trichrome staining was employed to accomplish CAM's histological investigation. As seen in Fig. 5 g, the egg treated with FL contain bioactive agent had larger CAM and denser, thicker collagen bundles when compared to egg treated with O-AlgCatCMCs-Ga and control. Moreover, compared to the control, the thickness of CAM in the FL treated group was substantially higher. It has been reported that increase in CAM thickness shows that fibroblasts are being stimulated and activated, which increases the production of collagen [23].

3.8. In vitro cytocompatibility and cell migration

Cytocompatibility is an essential parameter for wound healing. On the first day of culture, no significant differences between the cell viability of O-AlgCatCMCs, O-AlgCatCMCs-Ga, and BSS were noticed. Compared with the O-AlgCatCMCs-Ga and O-AlgCatCMCs, the BSS had notable proliferative trend over five days ($p \leq 0.01$), indicating the satisfactory cytocompatibility of BSS. Notably, both O-AlgCatCMCs-Ga and O-AlgCatCMCs were nontoxic for L929 cells' growth and proliferation, as the number of cells increased over time. Interestingly, cell number on the surface of O-AlgCatCMCs was lower than that of O-AlgCatCMCs-Ga. It can be attributed to slower degradation of O-AlgCatCMCs-Ga, which takes benefit of both Schiff-base and coordination bond. However, faster degradation of O-AlgCatCMCs with single Schiff-base bond in culture media not only could negatively affect cell adhesion and proliferation, but also disturb nutrient availability for cells. As obvious in Fig. 6 a, at day 1, 3, and 5 of culture, most of the cells in the experimental and control groups expressed green fluorescence with fair distribution, with few dead cells. It was observed that when number of cells increased, dead cells also followed the same trend but significantly lower in number, which can be due to scarcity of nutrients and space. The CCK-8 result was in line with fluorescent staining Fig. 6 b. Our results demonstrated higher proliferation rate of L929 fibroblast cells in

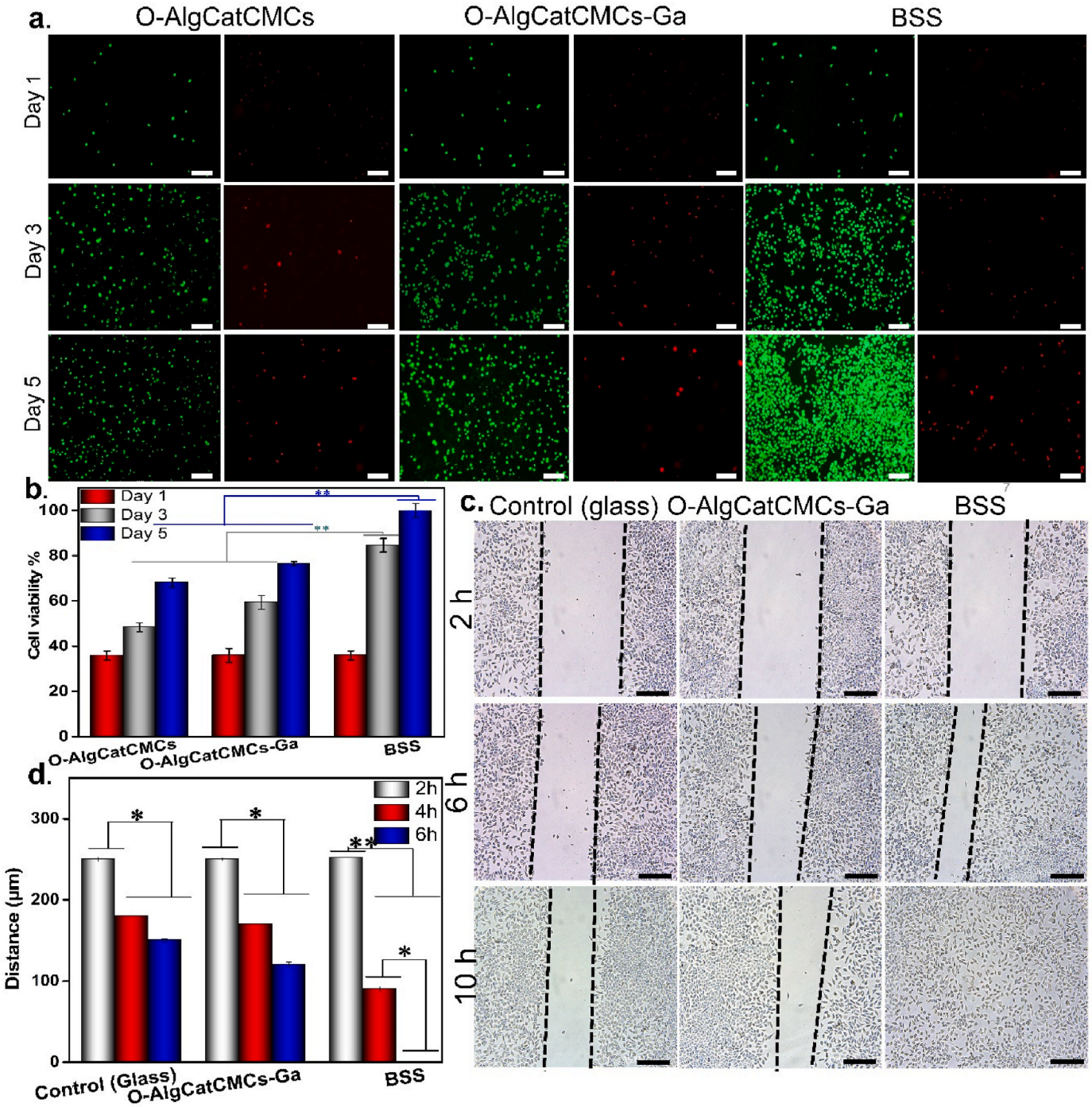

Fig. 6. *In vitro* cytocompatibility, and migration, capability of the BSS compared to O-AlgCatCMCs-Ga and control. (a) Live/Dead staining of L929 cells coculturing with the hydrogels for 1, 3, and 5 days, (Scale bar = 100 μm). (b) Proliferation of L929 cells with the hydrogels for 1, 3, and 5 days examined via CCK-8. (c) Scratch assay of BSS cells with the hydrogels for 2, 6 and 10 h, (Scale bar = 100 μm). (d) Quantitative analysis of the wound healing rates of L929 cells analyzed using scratch assay. *$p \leq 0.05$, **$p \leq 0.01$.

presence of biologically active BSS, which could be ascribed to the release of PDGF. Mirhaj et al. [66] have reported that PDGF had direct and notable effect on fibroblast proliferation and migration, which was coinciding our observation (Fig. 6).

It has been demonstrated that enhanced cell migration promotes wound healing [68]. The scratch assay is used to assess the migration capability of L929 cells. The images and quantitative findings from this experiment were analyzed after 2, 6, and 10 h. Cell mobility was significantly higher in cell contacted with BSS containing PRF and after 10 h ($p \leq 0.05$), with uniform distribution of cells (Fig. 6c). Compared with the BSS containing PRF, cells incubated with O-AlgCatCMCs-Ga showed slower cell mobility, followed by control. This trend persisted after 2, 6, and 10 h (Fig. 6d).

Several studies proved that bioactive PRF could positively affect cell growth, proliferation, migration, and differentiation of various cell lines. This property of PRF was accredited to the strong mitogen PDGF released [66].

PRF mainly consists platelets surrounded by strong fibrin filaments, various growth factors such as PDGF, IGF, TGF-β, and VEGF, and optimal amounts of thrombin [69]. The above-mentioned GFs promote

cell growth and proliferation and it has been reported that PRF not only contains GFs but also could trigger their secretion. A chemotactic effect occurs by GFs in PRF, which is the main reason of cell migration. Besides, thrombin promotes the migration of endothelial cells and fibroblasts, ultimately enhancing angiogenesis.

3.9. *In vivo infected burn wound healing*

Round-shaped, infected burned wounds with 0.7 mm diameter were created on dorsal region of male SD rats and treated differently with commercial SSD, BSS, and an untreated wound was also considered as a control. Photographs of these three groups on day 0, 6, and 12 were depicted in Fig. 7 a, indicating gradual reduction in wound size over time in all mice. Redness, swelling, and infection occurred around the untreated and the SSD-covered groups on day 6. Infection in both control and SSD-treated wounds had smell, though it was more visible as yellow-brown pus in control group due to lack of any treatment coverage. In contrast, the wounds treated with the bioactive BSS showed little redness, swelling, and no obvious signs of infection was observed, which was credited to the excellent antibacterial property and anti-infectious ability of the BSS. All above-mentioned observations demonstrated that the inflammatory period of the bioactive BSS-treated group was shorter than both control and SSD-treated group which results in faster wound closure (Fig. 7b). Additionally, wound closure traces were statistically analyzed and presented in Fig. 7 c. The BSS-treated wound had a significantly smaller wound area on day 6 (with closer rate of 60 ± 3%) than the control (with closer rate of 36 ± 5%) and SSD groups (with closer rate of 31 ± 4%). On day 12, the wound area of each group decreased significantly with healing rate of 58 ± 4, and 67 ± 5, for control and SSD, respectively, but the bioactive BSS-treated wound exhibited faster rate of healing, which was almost closed with some hair coverage. The control and SSD-covered wound were monitored till complete healing, which was 18 and 20 days for SSD and control group, respectively (Fig. 7d). Cotton gauze was used as a secondary dressing for SSD-covered wound to keep the wound area warm as well as fixing SSD in wound area. The wounds extensively secreted exudate, which was absorbed by cotton gauze and made it stick to wound area, although it was removed slowly for wound observation, but it caused tissue removal and pain. The natural healing time of the control group was around 20 days, and the BSS shortened the healing period of the burn wounds in mice to 12 days.

The results demonstrated that the bioactive BSS outperformed the SSD in accelerating wound closure even after 6 days, which could be attributed to its bilayer structure, avoiding bacterial penetration, no need of secondary dressing, and antibacterial activity of BSS that fights against environmental bacteria. Additionally, the impressive antibacterial activity of FL also destroyed bacteria already present in infected burn wound and bacterial debris and wound fluid could be efficiently absorbed by BSS or phagocytosed by neutrophils. More importantly, faster healing was granted by PRF release over time which was proven to promote angiogenesis, cell proliferation, and migration due to release of PDGF and VEGF (Fig. 4 f and g) [66].

3.10. *Histological analysis of regenerative skin tissue*

Histological analysis of regenerating skin tissue was performed to assess the therapeutic efficacy of the BSS for the treatment of infected wounds during the healing process (Fig. 8). According to the findings of H&E staining on day 6 after treatment, each group's epidermal (EP) structures displayed clear defects. Granulation tissue (G.T.) was observed in all groups and because of infection, the inflammatory cells (I·C) infiltration was more pronounced in the G.T. and adjacent EP regions in control and SSD groups. There were fewer I·C in the wound that was covered with BSS because of its outstanding antibacterial activity, which kills the bacteria and stops the inflammatory reactions (Fig. 8a). Yet, inflammation persisted in SSD-treated and control up to day 12. Additionally, neovascularization (N·V) was observed in wound covered by BSS at day 6 which increased significantly by day 12 indicating quicker skin tissue repair throughout that period compared to other groups (Fig. 8a). Resultantly, it can be concluded that the wound treated with bioactive BSS has already passed the inflammatory phase. It can also be possible that the ideal hemostatic property of BSS precedes the onset of inflammatory phase, followed by strong antibacterial activity and reduced inflammatory cells. Furthermore, bacteria in the wound are the primary cause of inflammation. They can be killed by antibacterial agents or trapped by neutrophils, subsequently macrophage M1 stops secreting interleukin (IL) and tumor necrosis factor (TNF) (proinflammatory cytokines) and turns to M2 macrophage, which plays an

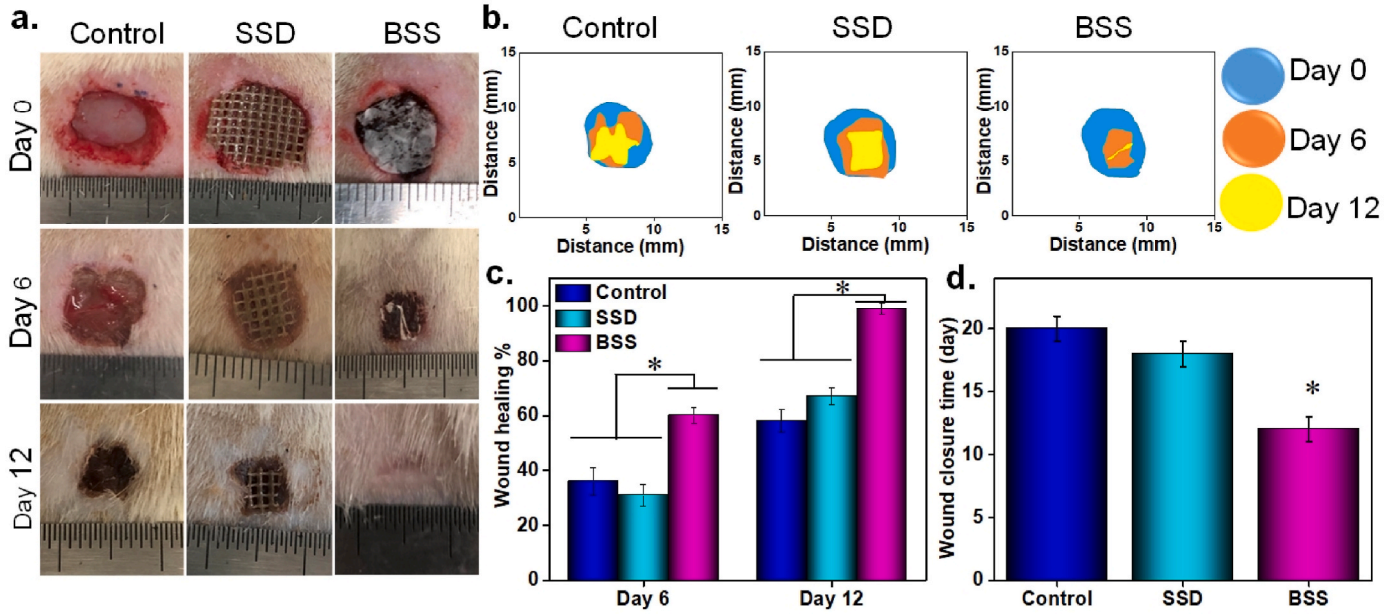

Fig. 7. *In vivo* infected burned wound healing studies of the BSS, commercial SSD and control (without treatment), (a) Visual photograph of the wound over 12 days, (b) Representative images of wound tissues and the area traces of wound closure treated with the BSS, commercial SSD and control on days 0, 6, and 12, (c) Quantitative analysis of mean healing rate in different groups for 0, 6, and 12 days, (d) Complete wound closure times for various treatments, *p ≤ 0.05.

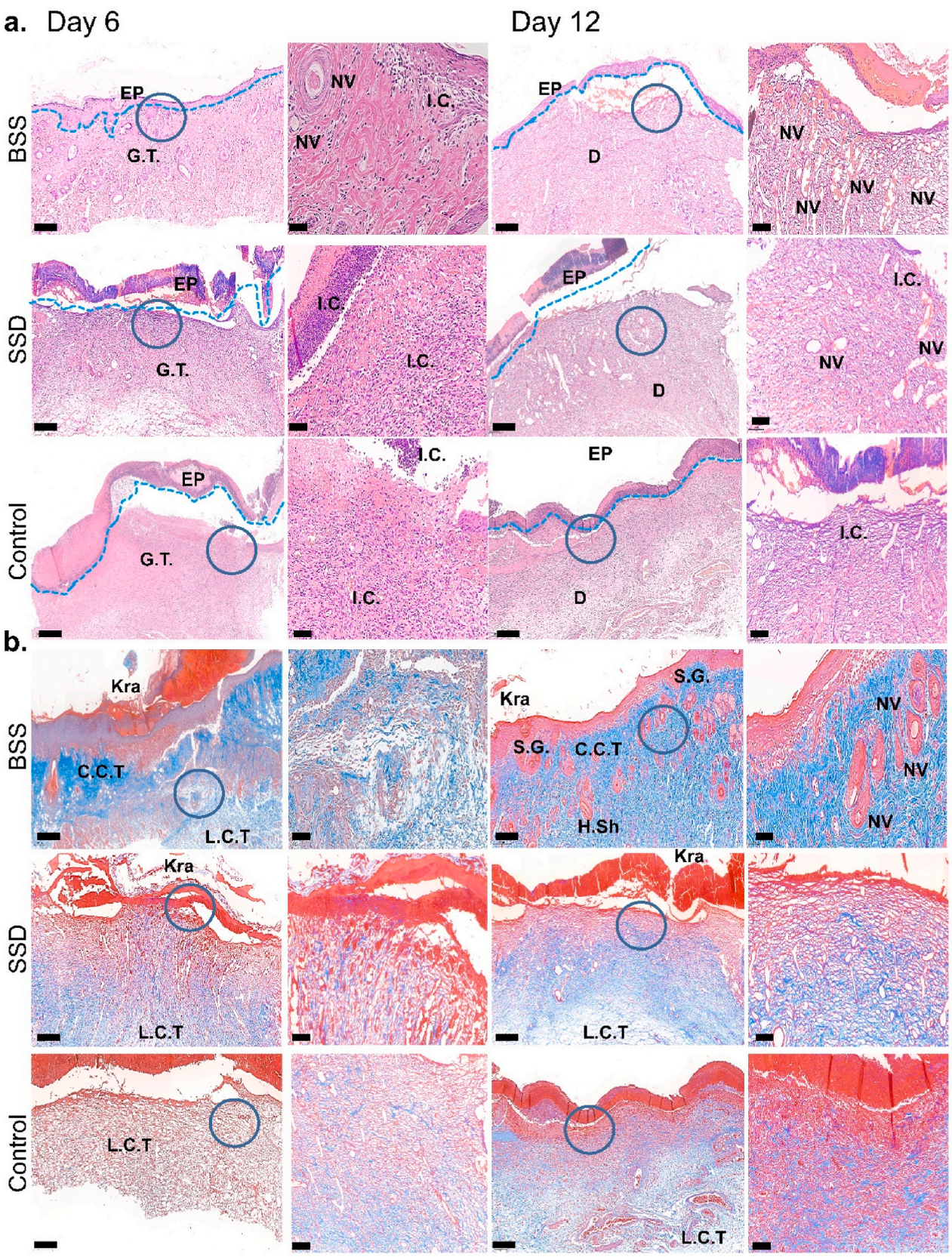

Fig. 8. Histological analysis of regenerative skin tissue, stained with (a) H&E and (b) Masson at day 6 and 12. Scale bare = 200 and 50 μm. G.T: Granular Tissue, EP: epidermal layer, NV: Neovascularization, L.C.T: Loose Connective Tissue, C·C.T: Compact Connective Tissue, S.G: Sebaceous Gland, Kra: Keratin layer and H. Sh: Hair Shaft.

important role in the remodeling of wound [70]. PRF has been shown to have anti-inflammatory properties. Due to release of TGFβ, PFR may reduce the expression of the M1 marker genes, interleukin 1β (IL1β), and interleukin 6 (IL6). Subsequently, PRF could assist in M1 to M2 transition [71]. This process was completed in BSS-covered wound. Whereas, ongoing inflammation was seen in control and SSD group, where more neutrophils exiting the blood vessels, fighting bacteria, and no M1 to M2 macrophage conversion (Fig. 8a).

On day 12 of the treatment, each group developed an EP layer and dermal (D) structure. The reconstruction of functional skin had started in the bioactive BSS-treated group, with distinct epithelial and normal-tissue-like structure observed. In contrast, the control group was still in the phase of epithelial regeneration with slight inflammatory cells and the SSD group was in the transition period between these two phases. Compared with the control and SSD groups, the reconstituted epithelium of the BSS-treated group was the thinnest. The process of reepithelization refers to transformation from an immature thicker epithelium to a mature thinner epithelium [72]. This result indicated that the re-epithelialization of the BSS-treated group was the fastest. The bioactive BSS-treated group exhibited a highest number of newly formed blood vessels (Fig. 8a). The findings revealed that the BSS promoted the proliferation and migration of keratinocytes, promoted epidermal remodeling, and accelerated the wound healing process.

Masson staining results demonstrated that collagen fibrils were deposited in the cutaneous tissues in control and BSS-treated group, but the collagen density was notably low in SSD treated and control group at day 6 (Fig. 8b). It has been reported that loose connective tissue (L.C.T) is related to low density collagen fibers and compact connective tissue (C·C.T) forms when high collagen density is synthesized [71]. L.C.T was observed in control and SSD-treated group with low collagen density. However, the BSS-treated group had both L.C.T and C·C.T at day 6, which turned to C·C.T at day 12. A complete epidermis structure with keratinized layer (Kra) was formed together with sebaceous glands (S. G.), hair Shaft (H.Sh) and blood vessels on day 12, where the wound was treated with BSS. Additionally, the regenerated skins were almost intact with numerous hair follicles in the healing region and well-arranged collagen deposition with dense and aligned fibers was also observed indicating that BSS could promote skin regeneration. Contrarily, collagen depositions were incompact in both control and commercial SSD-treated group (Fig. 8b).

The faster and higher density collagen production in bioactive BSS-treated group could be attributed to presence of PRF. PRF is reported to directly affect fibroblasts via PDGF release and moderately increase the expression of collagen type 1 [71].

3.11. Proinflammatory cytokines expression in regenerative skin tissue

Following tissue damage, a cascade of skin cell lysis is reported to be activated, where tissue-resident macrophages and damaged keratinocytes secrete TNF and IL-6. IL-6 is a soluble mediator with a pleiotropic effect on inflammation, immune response, and hematopoiesis [73]. Bacterial infection can augment IL-6 secretion, which can be used as molecular marker for infection [7]. TNF is a pro-inflammatory cytokine released by macrophages in response to the microbial lipopolysaccharide [74]. Inflammatory responses during the early stages of healing are linked to common proinflammatory cytokines including IL-6 and TNF-α [75]. Inflammation reactions persist as a result of bacterial infection by inhibiting M1 to M2 conversion of macrophages. According to reports, the middle and later phases of inflammation occur during usual wound healing process on day 6 [76]. The immunofluorescence staining disclosed that the control and SSD-treated group experienced a strong inflammatory reaction, whereas the BSS treated group displayed reduced levels of IL-6 and TNF-α expression (Fig. 9a). This outcome confirmed that BSS can effectively reduce inflammation. The substantial hemostasis and significant antibacterial activity of BSS, which shortens both hemostasis and inflammatory phases, can be credited for lower IL-6 and TNF-α level in BSS treated group. Moreover, bioactive BSS not only sealed the wound due to catechol group but also prevented germy entry in wound with its BL, accelerating the healing process.

The BSS-covered wound had lower inflammation, which was confirmed visually by reduced redness, swelling (Fig. 7a), and lower secretion of IL and TNF at molecular level confirmed by immunofluorescence staining (Fig. 9a).

3.12. Neovascularization analysis of regenerative skin tissue

Considering the fact that burned wounds lose more blood than other types of wounds, neovascularization is an essential aspect of burned wound healing. Neovascularization is promoted by faster dermal regeneration and tissue formation, which can be detected *in vivo* using VEGF as an indicator. On day 6 and 12, the highest VEGF expression was found in the tissue harvested from wound treated with BSS Fig. 9c and d. Immunofluorescence staining for CD-31 (vascular endothelial-specific marker) was employed to assess neovascularization. As shown in Fig. 9b and d, the expression level of CD-31 in the BSS-treated group on day 6 and 12 was significantly ($p \leq 0.01$) higher than in the other groups. The results demonstrated that the BSS had better pro-vascularization ability due to the release of PRF, which has been proven to induce angiogenesis [77]. The potential of better pro-vascularization formation makes BSS more favorable to promote the three-dimensional assembly of vascular networks, provide nutrition for epithelial regeneration, accelerate the process of re-epithelialization, and significantly improve wound healing. In comparison to SSD dressing, a commonly used commercial burn dressing, the BSS significantly accelerated wound closure, promoted skin structure reconstruction, prevented wound infection, encouraged the regeneration of blood vessels, and had better therapeutic efficacy on infected burn wounds.

4. Conclusion

Herein, we proposed that the fabricated BSS, which contains biologically active agent, could be used as an efficient treatment for infected burned wounds without the need of secondary coverage. Bioactive BSS is composed of BL and FL, where BL is hydrophobic, antibacterial and biodegradable, avoiding fluid entry into the wounded area and preventing bacterial invasion by killing them. FL was also formed via double cross linking of Schiff-base and reversible coordination of O-Alg-Ga to achieve desirable biodegradability. FL contained catechol group for better adhesion, PRF that can actively interact with blood cells etc., as a source of GFs, and gallium ion responsible for its antibacterial activity. The fabricated bioactive BSS demonstrated strong adhesion, significant bactericidal activity (by rupturing bacterial cell wall), faster clot formation, good cytocompatibility, and biodegradability. Additionally, the gallium could be released in pH-responsive manner which is promising for infected wounds treatment. The therapeutic efficacy of the as-synthesized BSS on infected burn wound healing was evaluated by *in vivo* infected burn rat models. Bioactive BSS exhibited a shorter healing time and a more complete skin structure with thinner epithelium and more hair follicles, as well as lower expression of proinflammatory cytokines, higher expression of VEGF, better angiogenesis and collagen deposition than commercial SSD. Furthermore, strong adhesiveness makes the fabricated bioactive BSS suitable for dynamic wounds with high frequency movement.

All these findings demonstrated that the multifunctional BSS had ideal therapeutic efficacy on infected burned wound healing and can be a promising candidate for infected burn wound treatment.

Ethics approval stand consent to participate

The animal study in this research was conducted strictly following the Laboratory Animal Ethics Review Committee of Donghua University (DHUEC-MOST-2021-06).

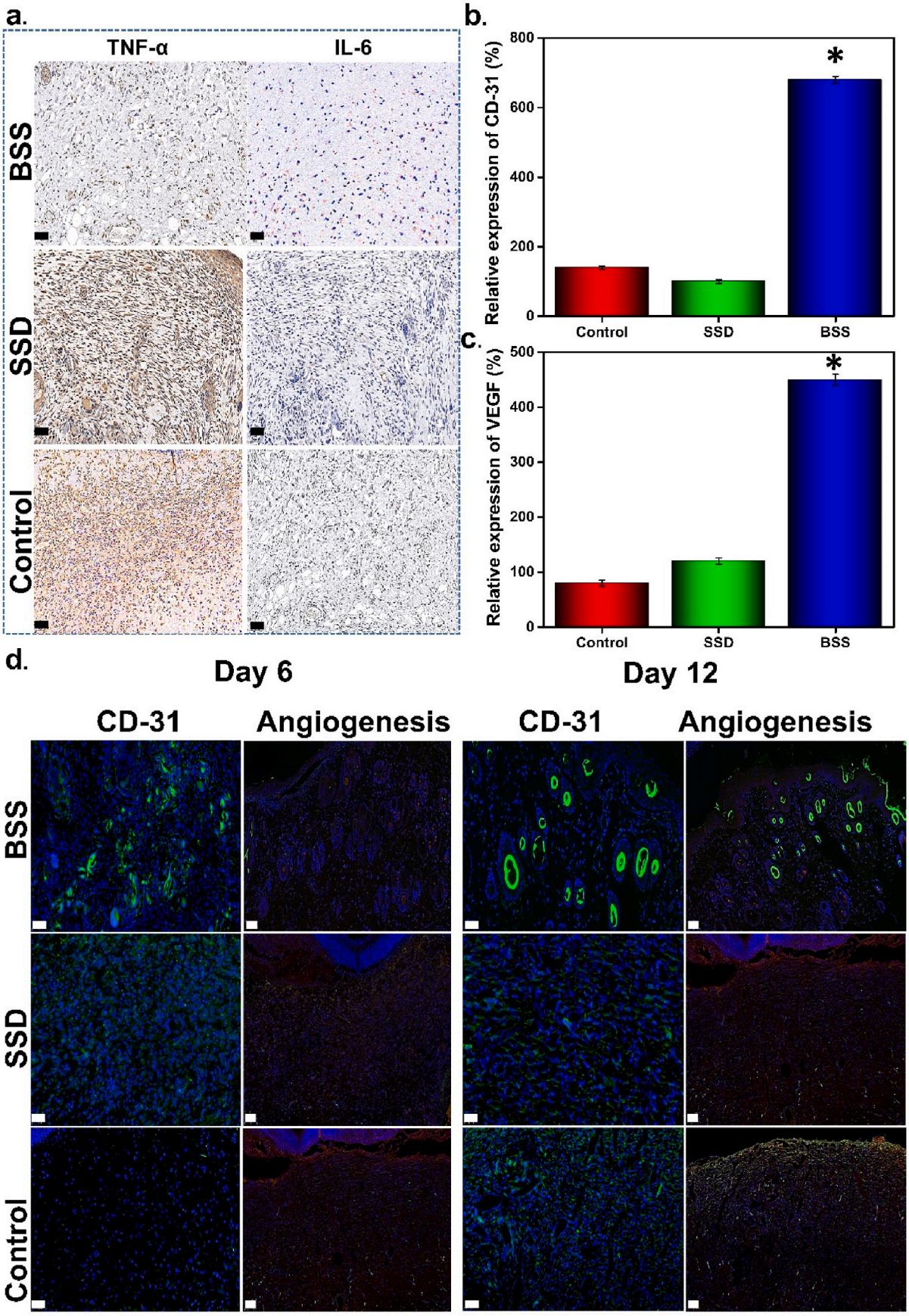
a.
TNF-α
IL-6
BSS
SSD
Control
b.
Relative expression of CD-31 (%)
800
600
400
200
0
*
Control
SSD
BSS
c.
Relative expression of VEGF (%)
500
400
300
200
100
0
*
Control
SSD
BSS
d.
Day 6
Day 12
CD-31
Angiogenesis
CD-31
Angiogenesis
BSS
SSD
Control

Fig. 9. (A) Immunostaining of TNF-α and IL-6 on day 6 (scale bare = 100 μm), Quantified analysis of the relative expression of (b) CD-31 expression, and (c) VEGF, (d) Photographs of wound tissues after immunofluorescence staining for CD-31 expression, and VEGF detection at day 6 and 12 (scale bare 100 and 50 μm), *p ≤ 0.01.

CRediT authorship contribution statement

Mina Shahriari-Khalaji: Conceptualization, Data curation, Formal analysis, Funding acquisition, Resources, Validation, Writing – original draft, Writing – review & editing. **Mamoona Sattar:** Conceptualization, Data curation, Formal analysis, Funding acquisition, Resources, Validation, Writing – original draft, Writing – review & editing. **Ran Cao:** Conceptualization, Methodology and Investigation. **Meifang Zhu:** Methodology and Investigation.

Declaration of competing interest

Herein, the authors of manuscript entitled "Angiogenesis, hemocompatibility and bactericidal effect of bioactive natural polymer-based bilayer adhesive skin substitute for infected burned wound healing" declare that they have no known competing financial interests or personal relationships that could have appeared to influence the work reported in this paper.

Acknowledgments

This work is financially supported by the National Key Research and Development Program of China (2021YFA1201304/2021YFA1201300), the Fundamental Research Funds for the Central Universities (2232022D-01), the Science and Technology Commission of Shanghai Municipality, China (20DZ2254900), and the Young Elite Scientists Sponsorship Program by CAST (YESS20220259).

Appendix A. Supplementary data

Supplementary data to this article can be found online at https://doi.org/10.1016/j.bioactmat.2023.07.008.

References

[1] P.G. Manita, I. Garcia-Orue, E. Santos-Vizcaino, R.M. Hernandez, M. Igartua, 3D bioprinting of functional skin substitutes: from current achievements to future goals, Pharm. Times 14 (4) (2021) 362.
[2] Y. Yuan, S. Shen, D. Fan, A physicochemical double cross-linked multifunctional hydrogel for dynamic burn wound healing: shape adaptability, injectable self-healing property and enhanced adhesion, Biomaterials 276 (10) (2021), 120838.
[3] A.M. Lachiewicz, C.G. Hauck, D.J. Weber, B.A. Cairns, D. van Duin, Bacterial infections after burn injuries: impact of multidrug resistance, clinical infectious diseases : an official publication of the infectious diseases society of America, Clin. Infect. Dis. 65 (12) (2017) 2130–2136.
[4] A.u.R. Khan, K. Huang, M.S. Khalaji, F. Yu, X. Xie, T. Zhu, Y. Morsi, Z. Jinzhong, X. Mo, Multifunctional bioactive core-shell electrospun membrane capable to terminate inflammatory cycle and promote angiogenesis in diabetic wound, Bioact. Mater. 6 (9) (2021) 2783–2800.
[5] Y. Yang, X. Zhao, J. Yu, X. Chen, R. Wang, M. Zhang, Q. Zhang, Y. Zhang, S. Wang, Y. Cheng, Bioactive skin-mimicking hydrogel band-aids for diabetic wound healing and infectious skin incision treatment, Bioact. Mater. 6 (11) (2021) 3962–3975.
[6] A. Przekora, A concise review on tissue engineered artificial skin grafts for chronic wound treatment: can we reconstruct functional skin tissue *in vitro*, Cells 9 (7) (2020) 1622.
[7] S. Yao, Y. Zhao, Y. Xu, B. Jin, M. Wang, C. Yu, Z. Guo, S. Jiang, R. Tang, X. Fang, S. Fan, Injectable dual-dynamic-bond cross-linked hydrogel for highly efficient infected diabetic wound healing, Adv. Healthc. Mater. 11 (14) (2022), e2200516.
[8] W. Zhang, R. Wang, Z. Sun, X. Zhu, Q. Zhao, T. Zhang, A. Cholewinski, F.K. Yang, B. Zhao, R. Pinnaratip, P.K. Forooshani, B.P. Lee, Catechol-functionalized hydrogels: biomimetic design, adhesion mechanism, and biomedical applications, Chem. Soc. Rev. 49 (2) (2020) 433–464.
[9] B.P. Lee, P.B. Messersmith, J.N. Israelachvili, J.H. Waite, Mussel-inspired adhesives and coatings, Annu. Rev. Mater. Res. 41 (3) (2011) 99–132.
[10] L. Han, X. Lu, K. Liu, K. Wang, L. Fang, L.T. Weng, H. Zhang, Y. Tang, F. Ren, C. Zhao, G. Sun, R. Liang, Z. Li, Mussel-inspired adhesive and tough hydrogel based on nanoclay confined dopamine polymerization, ACS Nano 11 (3) (2017) 2561–2574.
[11] H. Lee, S.M. Dellatore, W.M. Miller, P.B. Messersmith, Mussel-inspired surface chemistry for multifunctional coatings, Science 318 (5849) (2007) 426–430.
[12] J. Cui, Y. Yan, G.K. Such, K. Liang, C.J. Ochs, A. Postma, F. Caruso, Immobilization and intracellular delivery of an anticancer drug using mussel-inspired polydopamine capsules, Biomacromolecules 13 (8) (2012) 2225–2228.
[13] W. Zhang, R. Wang, Z. Sun, X. Zhu, Q. Zhao, T. Zhang, A. Cholewinski, F. Yang, B. Zhao, R. Pinnaratip, P.K. Forooshani, B.P. Lee, Catechol-functionalized hydrogels: biomimetic design, adhesion mechanism, and biomedical applications, Chem. Soc. Rev. 49 (2) (2020) 433–464.
[14] T. Chen, Y. Chen, H.U. Rehman, Z. Chen, Z. Yang, M. Wang, H. Li, H. Liu, Ultratough, self-healing, and tissue-adhesive hydrogel for wound dressing, ACS appl. Mater. Inter. 10 (39) (2018) 33523–33531.
[15] L. Han, L. Yan, K. Wang, L. Fang, H. Zhang, Y. Tang, Y. Ding, L.-T. Weng, J. Xu, J. Weng, Y. Liu, F. Ren, X. Lu, Tough, self-healable and tissue-adhesive hydrogel with tunable multifunctionality, NPG Asia Mater. 9 (4) (2017) e372-e372.
[16] M. Shahriari-Khalaji, A. Alassod, Z. Nozhat, Cotton-based health care textile: a mini review, Polym. Bull. 79 (10) (2022) 1–24.
[17] D.R. Sahoo, T. Biswal, Alginate and its application to tissue engineering, SN Appl. Sci. 3 (1) (2021) 30.
[18] K.H. Bouhadir, K.Y. Lee, E. Alsberg, K.L. Damm, K.W. Anderson, D.J. Mooney, Degradation of partially oxidized alginate and its potential application for tissue engineering, Biotechnol. 17 (5) (2001) 945–950.
[19] W. Ding, J. Zhou, Y. Zeng, Y.-n. Wang, B. Shi, Preparation of oxidized sodium alginate with different molecular weights and its application for crosslinking collagen fiber, Carbohydr. Polym. 157 (2) (2017) 1650–1656.
[20] J. Li, X. Wu, Y. Wu, Z. Tang, X. Sun, M. Pan, Y. Chen, J. Li, R. Xiao, Z. Wang, H. Liu, Porous chitosan microspheres for application as quick in vitro and in vivo hemostat, Mat. Sci. Eng. C, Mater. 77 (2) (2017) 411–419.
[21] M. Xie, Y. Zeng, H. Wu, S. Wang, J. Zhao, Multifunctional carboxymethyl chitosan/oxidized dextran/sodium alginate hydrogels as dressing for hemostasis and closure of infected wounds, Int. J. Biol. Macromol. 219 (4) (2022) 1337–1350.
[22] L. Ma, Y. Tan, X. Chen, Y. Ran, Q. Tong, L. Tang, W. Su, X. Wang, X. Li, Injectable oxidized alginate/carboxylmethyl chitosan hydrogels functionalized with nanoparticles for wound repair, Carbohydr. Polym. 293 (6) (2022), 119733.
[23] M. Tavakoli, M. Mirhaj, S. Salehi, J. Varshosaz, S. Labbaf, A. Golshirazi, N. Kazemi, V. Haghighi, Coaxial electrospun angiogenic nanofiber wound dressing containing advanced platelet rich-fibrin, Int. J. Biol. Macromol. 222 (3) (2022) 1605–1618.
[24] F. Tabatabaei, Z. Aghamohammadi, L. Tayebi, *In vitro* and *in vivo* effects of concentrated growth factor on cells and tissues, J. Biomed. 108 (6) (2020) 1338–1350.
[25] M. Mirhaj, M. Tavakoli, J. Varshosaz, S. Labbaf, F. Jafarpour, P. Ahmaditabar, S. Salehi, N. Kazemi, Platelet rich fibrin containing nanofibrous dressing for wound healing application: fabrication, characterization and biological evaluations, Mater. Sci. Eng. C 22 (A) (2021), 112541.
[26] M. Tavakoli, M. Mirhaj, S. Labbaf, J. Varshosaz, S. Taymori, F. Jafarpour, S. Salehi, S.A.M. Abadi, A. Sepyani, Fabrication and evaluation of Cs/PVP sponge containing platelet-rich fibrin as a wound healing accelerator: an *in vitro* and *in vivo* study, Int. J. Biol. Macromol. 204 (4) (2022) 245–257.
[27] Y. Fan, K. Perez, H. Dym, Clinical uses of platelet-rich fibrin in oral and maxillofacial surgery, Dent. Clin. 64 (2) (2020) 291–303.
[28] F. Li, F. Liu, K. Huang, S. Yang, Advancement of gallium and gallium-based compounds as antimicrobial agents, Front. Bioeng. Biotechnol. 10 (5) (2022), 827960.
[29] M. Shahriari-Khalaji, F. Zabihi, A. Bahi, D. Sredojević, J.M. Nedeljković, D. K. Macharia, M. Ciprian, S. Yang, F. Ko, Photon-driven bactericidal performance of surface-modified TiO_2 nanofibers, J. Mater. Chem. C. 11 (17) (2023) 5796–5805.
[30] X. Zhang, C. Shi, Z. Liu, F. Pan, R. Meng, X. Bu, H. Xing, Y. Deng, N. Guo, L. Yu, Antibacterial activity and mode of action of ε-polylysine against *Escherichia coli* O157:H7, J. Med. Microbiol. 67 (6) (2018) 838–845.
[31] T. Distler, A.A. Solisito, D. Schneidereit, O. Friedrich, R. Detsch, A.R. Boccaccini, 3D printed oxidized alginate-gelatin bioink provides guidance for C2C12 muscle precursor cell orientation and differentiation via shear stress during bioprinting, Biofabrication 12 (4) (2020), 045005.
[32] C. Lee, J. Shin, J.S. Lee, E. Byun, J.H. Ryu, S.H. Um, D.-I. Kim, H. Lee, S.-W. Cho, Bioinspired, calcium-free alginate hydrogels with tunable physical and mechanical properties and improved biocompatibility, Biomacromolecules 14 (6) (2013) 2004–2013.
[33] L. Yuan, Y. Wu, J. Fang, X. Wei, Q. Gu, H. El-Hamshary, S.S. Al-Deyab, Y. Morsi, X. Mo, Modified alginate and gelatin cross-linked hydrogels for soft tissue adhesive, Artif. Cells, Nanomed. Biotechnol. 45 (1) (2017) 76–83.
[34] H. Yuan, L. Chen, F.F. Hong, A biodegradable antibacterial nanocomposite based on oxidized bacterial nanocellulose for rapid hemostasis and wound healing, ACS Appl. Mater. Interfaces 12 (3) (2020) 3382–3392.
[35] P. Zhang, L. Chen, Q. Zhang, F.F. Hong, Using in situ dynamic cultures to rapidly biofabricate fabric-reinforced composites of chitosan/bacterial nanocellulose for antibacterial wound dressings, Front. Microbiol. 7 (4) (2016), 260-260.
[36] M. Shahriari-Khalaji, G. Hu, L. Chen, Z. Cao, T. Andreeva, X. Xiong, R. Krastev, F. F. Hong, Functionalization of aminoalkylsilane-grafted bacterial nanocellulose with ZnO-NPps-doped pullulan electrospun nanofibers for multifunctional wound dressing, ACS Biomater. Sci. Eng. 7 (8) (2021) 3933–3946.

[37] M. Shahriari-Khalaji, G. Li, L. Liu, M. Sattar, L. Chen, C. Zhong, F.F. Hong, A poly-l-lysine-bonded TEMPO-oxidized bacterial nanocellulose-based antibacterial dressing for infected wound treatment, Carbohydr. Polym. 287 (4) (2022), 119266.
[38] E. Anitua, M. Sanchez, J. Merayo-Lloves, M. Fuente, F. Muruzabal, G. Orive, Plasma rich in growth factors (prgf-endoret) stimulates proliferation and migration of primary keratocytes and conjunctival fibroblasts and inhibits and reverts TGF- 1-induced myodifferentiation, Invest. Ophthalmol. Vis. Sci. 52 (8) (2011) 6066–6073.
[39] J.H. Teoh, A. Mozhi, V. Sunil, S.M. Tay, J. Fuh, C.-H. Wang, 3D printing personalized, photocrosslinkable hydrogel wound dressings for the treatment of thermal burns, Adv. Funct. Mater. 31 (48) (2021), 2105932.
[40] T. Distler, K. McDonald, S. Heid, E. Karakaya, R. Detsch, A.R. Boccaccini, Ionically and enzymatically dual cross-linked oxidized alginate gelatin hydrogels with tunable stiffness and degradation behavior for tissue engineering, ACS Biomater. Sci. Eng. 6 (7) (2020) 3899–3914.
[41] H. Wang, X. Chen, Y. Wen, D. Li, X. Sun, Z. Liu, H. Yan, Q. Lin, A study on the correlation between the oxidation degree of oxidized sodium alginate on its degradability and gelation, Polymers 14 (9) (2022) 1679.
[42] M.K. Ku, Y. Ahn, Y. Song, Y.-H. Yang, H. Kim, Effect of oxidized alginate on its electrospinnability, Fibers Polym. 15 (9) (2014) 1835–1841.
[43] W. Ma, W. Dong, S. Zhao, T. Du, Y. Wang, J. Yao, Z. Liu, D. Sun, M. Zhang, An injectable adhesive antibacterial hydrogel wound dressing for infected skin wounds, Biomater. Adv. 134 (3) (2022), 112584.
[44] W. Su, Y. Ran, L. Ma, X. Ma, Z. Yih, G. Chen, X. Chen, Z. Deng, Q. Tong, X. Li, Micro-/nanomechanics dependence of biomimetic matrices upon collagen-based fibrillar aggregation and arrangement, Biomacromolecules 21 (3) (2020) 3547–3560.
[45] Z. Emami, M. Ehsani, M. Zandi, R. Foudazi, Controlling alginate oxidation conditions for making alginate-gelatin hydrogels, Carbohydr. Polym. 198 (7) (2018) 509–517.
[46] I. Janković, Z. Saponjic, E. Džunuzović, J. Nedeljković, New hybrid properties of TiO_2 nanoparticles surface modified with catecholate type ligands, Nanoscale Res. Lett. 5 (2) (2009) 81–88.
[47] Z. Naghizadeh, A. Karkhaneh, A. Khojasteh, Self-crosslinking effect of chitosan and gelatin on alginate based hydrogels: injectable in situ forming scaffolds, Mat. Sci. Eng. C-Mater. 89 (5) (2018) 256–264.
[48] J. Saiz-Poseu, J. Mancebo-Aracil, F. Nador, F. Busqué, D. Ruiz-Molina, The chemistry behind catechol-based adhesion, Angew. Chem. 58 (3) (2019) 696–714.
[49] K. Kim, K. Kim, J.H. Ryu, H. Lee, Chitosan-catechol: a polymer with long-lasting mucoadhesive properties, Biomaterials 52 (6) (2015) 161–170.
[50] J. Qin, M. Li, M. Yuan, X. Shi, J. Song, Y. He, H. Mao, D. Kong, Z. Gu, Gallium(III)-mediated dual-cross-linked alginate hydrogels with antibacterial properties for promoting infected wound healing, ACS Appl. Mater. Interfaces 14 (19) (2022) 22426–22442.
[51] M. Shahriari-Khalaji, S. Hong, G. Hu, Y. Ji, F.F. Hong, Bacterial nanocellulose-enhanced alginate double-network hydrogels cross-linked with six metal cations for antibacterial wound dressing, Polymers 12 (11) (2020) 2683.
[52] R. Miron, M. Bishara, J. Choukroun, Course number: 208 Basics of platelet-rich fibrin therapy, Dent. Today 36 (4) (2017), 309062.
[53] Z. Xu, X. Zhao, X. Chen, Z. Chen, Z. Xia, Antimicrobial effect of gallium nitrate against bacteria encountered in burn wound infections, RSC Adv. 7 (82) (2017) 52266–52273.
[54] M. Wynn, The impact of infection on the four stages of acute wound healing: an overview, Wounds U. K. 17 (5) (2021) 6–90.
[55] A.B. Castro, E.R. Herrero, V. Slomka, N. Pinto, W. Teughels, M. Quirynen, Antimicrobial capacity of leucocyte-and platelet rich fibrin against periodontal pathogens, Sci. Rep. 9 (1) (2019) 8188.
[56] L. Wang, X. Zhang, K. Yang, Y.V. Fu, T. Xu, S. Li, D. Zhang, L.-N. Wang, C.-S. Lee, A novel double-crosslinking-double-network design for injectable hydrogels with enhanced tissue adhesion and antibacterial capability for wound treatment, Adv. Funct. Mater. 30 (1) (2020), 1904156.
[57] H.T.P. Anh, C.-M. Huang, C.-J. Huang, Intelligent metal-phenolic metallogels as dressings for infected wounds, Sci. Rep. 9 (1) (2019), 11562.
[58] X. Zhang, R. Xu, X. Hu, G. Luo, J. Wu, W. He, A systematic and quantitative method for wound-dressing evaluation, Burns Trauma 3 (1) (2015) 15.
[59] E.M. Jones, C.A. Cochrane, S.L. Percival, The effect of pH on the extracellular matrix and biofilms, Adv. Wound Care 4 (7) (2015) 431–439.
[60] G. Gainza, S. Villullas, J.L. Pedraz, R.M. Hernandez, M. Igartua, Advances in drug delivery systems (DDSs) to release growth factors for wound healing and skin regeneration, Nano 11 (6) (2015) 1551–1573.
[61] P. Losi, E. Briganti, A. Magera, D. Spiller, C. Ristori, B. Battolla, M. Balderi, S. Kull, A. Balbarini, R. Di Stefano, G. Soldani, Tissue response to poly(ether)urethane-polydimethylsiloxane-fibrin composite scaffolds for controlled delivery of pro-angiogenic growth factors, Biomaterials 31 (20) (2010) 5336–5344.
[62] V. Andreu, G. Mendoza, M. Arruebo, S. Irusta, Smart dressings based on nanostructured fibers containing natural origin antimicrobial, anti-inflammatory, and regenerative compounds, Materials 8 (3) (2015) 5154–5193.
[63] H. Liu, C. Wang, C. Li, Y. Qin, Z. Wang, F. Yang, Z. Li, J. Wang, A functional chitosan-based hydrogel as a wound dressing and drug delivery system in the treatment of wound healing, RSC Adv. 8 (14) (2018) 7533–7549.
[64] T. Tsukioka, T. Hiratsuka, M. Nakamura, T. Watanabe, Y. Kitamura, K. Isobe, T. Okudera, H. Okudera, A. Azuma, K. Uematsu, K. Nakata, T. Kawase, An on-site preparable, novel bone-grafting complex consisting of human platelet-rich fibrin and porous particles made of a recombinant collagen-like protein: bone substitute consisting of synthetic rgd protein and PRF, J. of Biomed. 107 (3) (2019) 1420–1430.
[65] D. Ribatti, The chick embryo chorioallantoic membrane as a model for tumor biology, Exp. Cell Res. 328 (2) (2014) 314–324.
[66] M. Mirhaj, M. Tavakoli, J. Varshosaz, S. Labbaf, S. Salehi, A. Talebi, N. Kazemi, V. Haghighi, M. Alizadeh, Preparation of a biomimetic bi-layer chitosan wound dressing composed of A-PRF/sponge layer and L-arginine/nanofiber, Carbohydr. Polym. 292 (5) (2022), 119648.
[67] T. Ziebart, A. Schnell, C. Walter, P.W. Kämmerer, A. Pabst, K.M. Lehmann, J. Ziebart, M.O. Klein, B. Al-Nawas, Interactions between endothelial progenitor cells (EPC) and titanium implant surfaces, Clin. Oral Invest. 17 (1) (2013) 301–309.
[68] N. Ninan, A. Forget, V.P. Shastri, N.H. Voelcker, A. Blencowe, Antibacterial and anti-inflammatory pH-responsive tannic acid-carboxylated agarose composite hydrogels for wound healing, ACS Appl. Mater. Interfaces 8 (42) (2016) 28511–28521.
[69] M. Mirhaj, S. Labbaf, M. Tavakoli, A.M. Seifalian, Emerging treatment strategies in wound care, Int. Wound J. 19 (7) (2022) 1934–1954.
[70] L. Wang, X. Shang, X. Qi, D. Ba, J. Lv, X. Zhou, H. Wang, N. Shaxika, J. Wang, X. Ma, Clinical significance of M1/M2 macrophages and related cytokines in patients with spinal tuberculosis, Dis. Markers 45 (4) (2020), 2509454.
[71] J. Nasirzade, Z. Kargarpour, S. Hasannia, F.J. Strauss, R. Gruber, Platelet-rich fibrin elicits an anti-inflammatory response in macrophages *in vitro*, J. Periodontol. 91 (2) (2020) 244–252.
[72] P. Rousselle, F. Braye, G. Dayan, Re-epithelialization of adult skin wounds: cellular mechanisms and therapeutic strategies, Adv. Drug Deliv. 146 (9) (2019) 344–365.
[73] B.Z. Johnson, A.W. Stevenson, C.M. Prêle, M.W. Fear, F.M. Wood, The role of IL-6 in skin fibrosis and cutaneous wound healing, Biomedicines 8 (5) (2020) 101.
[74] J.F. Foley, No TNF-α; secretion without ERK activation, Sci. Signal. 1 (2) (2008), ec15.
[75] J. Qu, X. Zhao, Y. Liang, T. Zhang, P.X. Ma, B. Guo, Antibacterial adhesive injectable hydrogels with rapid self-healing, extensibility and compressibility as wound dressing for joints skin wound healing, Biomaterials 183 (6) (2018) 185–199.
[76] B. Zhang, J. He, M. Shi, Y. Liang, B. Guo, Injectable self-healing supramolecular hydrogels with conductivity and photo-thermal antibacterial activity to enhance complete skin regeneration, Chem. Eng. J. 400 (9) (2020), 125994.
[77] H. Weng, W. Jia, M. Li, Z. Chen, New injectable chitosan-hyaluronic acid based hydrogels for hemostasis and wound healing, Carbohydr. Polym. 294 (5) (2022), 119767.